Advancing cosmological statistics: From bispectrum multipole mixing to optimized projected correlation functions

by

Giorgi Khomeriki

B.S., Tbilisi State University, Georgia, 2020

A THESIS

submitted in partial fulfillment of the
requirements for the degree

MASTER OF SCIENCE

Department of Physics
College of Arts and Sciences

KANSAS STATE UNIVERSITY
Manhattan, Kansas

2026

Approved by:

Major Professor
Lado Samushia

Copyright

Abstract

This thesis presents advanced statistical tools and optimizations for the analysis of large-scale structure, focusing on the bispectrum and the projected correlation function. First, we derive general analytical expressions for how the Alcock-Paczynski distortions affect the power spectrum and bispectrum of cosmological fields. We compute explicit mixing coefficients for bispectrum multipoles in the linear approximation, demonstrating that the leading-order effect is a uniform dilation of the wavevector triplet. While the linear approximation is highly accurate for all power spectrum multipoles and the bispectrum monopole, we identify sub-percent level inaccuracies in the bispectrum quadrupole and a failure in the hexadecapole. These analytical results provide a rigorous alternative to numerical schemes, simplifying bispectrum analysis for galaxy surveys and the measurement of the baryon acoustic oscillation peak position.

Second, we investigate the optimization of projected correlation function analysis, specifically examining how results depend on the line-of-sight integration limit, pi-max. Utilizing varied halo occupation distribution parameters and cosmological models, we quantify the dependence of Fisher information on the choice of pi-max. We find that the optimal integration limits for maximizing information content often fall within non-standard ranges, spanning from 10 to 100 h-1 Mpc. Together, these studies enhance the precision of cosmological constraints by providing exact analytical frameworks for higher-order statistics and optimized configurations for projected clustering measurements.

Table of Contents

List of Figures

List of Tables

Chapter 1

Introduction

This thesis is composed of two primary research objectives. The first major component investigates the intricate mixing of galaxy bispectrum multipoles under geometric distortions. This work provides a rigorous framework for accounting for these distortions, which is essential for accurately recovering cosmological information from the anisotropic clustering of galaxies[2]. The second core objective of this work (that has not been published as a separate paper yet) focuses on the optimization of projected correlation functions, $w_p(r_p)$. By examining the stability of these measurements across various integration limits and utilizing high-accuracy simulation suites. Together, these two investigations offer novel methodologies for analyzing the next generation of spectroscopic galaxy surveys.

Geometric Distortions in Cosmological Surveys

By measuring redshifts and angular positions, galaxy surveys inherently document the placement of galaxies within spherical coordinates[3]. To transition these data into physical Cartesian coordinates, we must assume a specific expansion history and spatial curvature for the Universe. If the selected fiducial model deviates from the Universe's actual physics, the perceived distances between galaxies undergo distortion. These geometric shifts allow researchers to back-calculate the true cosmology from the initial fiducial assumptions.

Such distortions influence every statistical appraisal of large-scale structure. For instance, the observed power spectrum effectively becomes a warped variation of the actual power spectrum:

$$P^{\mathrm{m}}(k_{||}, k_{\perp}) = P^{\mathrm{t}}(\alpha_{||}[\mathbf{p}]k_{||}^{\mathrm{m}}, \alpha_{\perp}[\mathbf{p}]k_{\perp}^{\mathrm{m}}) \tag{1.1}$$

In this context, $\alpha_{||}$ and $\alpha_{\perp}$ represent distortion parameters along and perpendicular to the line of sight, respectively, dictated by the cosmological parameters $\mathbf{p}$. When the power spectrum contains a feature at a predefined wave number, $\mathbf{p}$ can be constrained by identifying the α values that align the measured feature with its theoretical location.

Parametrization and Features

Commonly, these distortions are characterized by α_V, which represents the total average distance distortion, and α_ϵ, which defines the differential warping between the line-of-sight and transverse planes[4–12]. Any isotropic measurement (or one with a well-defined initial anisotropy) is sensitive to α_ϵ, whereas measurements tied to a known physical scale provide sensitivity to α_V.

The Baryon Acoustic Oscillation (BAO) remains the premier distance scale utilized for this purpose. Arising from overdensity patterns in the early distribution of matter[13–15], the BAO has been detected in the two-point clustering of various galaxy populations. Currently, these detections offer the most robust constraints on the relationship between distance and redshift[16–21].

Alternative Probes

Beyond the BAO, several other methodologies have been employed to probe these parameters:

- **Cosmic Voids and Clustering:** Properties of cosmic voids[22–26] and the clustering between voids and galaxies[27–35].

- **Mapping and Forests:** The Lyman-α forest[36–38] and HI intensity mapping[34;39–45].

- **Novel Approaches:** Wavelet-transformed galaxy fields[46] and recent proposals to utilize the entire galaxy distribution as a comprehensive probe for distortion parameters[47;48].

The primary goal of this research is to explore the nuances of utilizing galaxy bispectrum (three-point correlation function) multipoles for measuring geometric distortions. As a function of density distribution, the galaxy bispectrum $B(k_1, k_2, k_{3,1}, \phi)$ depends on five distinct parameters[49;50]. For analytical convenience, it is frequently decomposed into spherical harmonics, $B_{\ell m}(k_1, k_2, k_3)$, across its angular arguments[51–54]. Theoretical forecasts indicate that incorporating bispectrum data can substantially improve cosmological constraints derived from the galaxy power spectrum alone[51;55–59].

Recent literature has leveraged the galaxy bispectrum to investigate various phenomena, including:

- **BAO and Anisotropy:** Determining BAO peak positions[60–63] and analyzing full anisotropic shapes[51;64–71]. Recent results from the Dark Energy Spectroscopic Instrument (DESI) have provided high-significance detections of the BAO signal in the three-point correlation function[72].

- **Baryonic and Primordial Physics:** Probing baryonic effects[73–76] and primordial non-Gaussianity (PNG)[77–82]. New research underscores the necessity of accounting for relativistic effects in the bispectrum to avoid biasing f_{NL} measurements in upcoming surveys[82].

- **Higher-Order Statistics:** Utilizing massive neutrinos probes[83], fourth-order clustering (trispectrum)[84–87], and parity-violating signatures in large-scale structure[88;89].

In these analyses, geometric distortions cause a mixing of multipoles that must be rigorously addressed. While modeling these distortions by direct rescaling of the bispectrum arguments is a straightforward solution, it is computationally prohibitive. Power and bispectrum models are typically evaluated via Markov Chain Monte Carlo (MCMC) simulations across high-dimensional parameter spaces[90–93]; re-calculating the bispectrum at every MCMC step is inefficient. A more streamlined approach involves estimating the warped bispectrum through a linear approximation, utilizing derivatives and precomputed moments from a fiducial cosmology. This technique is well-validated for power spectrum studies[94] and has recently been applied to bispectrum analyses[2;67]. Throughout this work, we adopt the plane-parallel approximation[95;96].

Projected Correlation Function

The primary objective of the second part of this work is to investigate the efficacy of the **projected correlation function**, $w_p(r_p)$, as a robust probe for cosmological parameters while mitigating the systematic effects of Redshift Space Distortions (RSD). Galaxy surveys record positions in redshift space, where peculiar velocities along the line-of-sight (LOS) introduce anisotropies in the clustering signal[97;98]. To isolate the real-space clustering, it is standard practice to integrate the two-dimensional correlation function $\xi(r_p, \pi)$ along the LOS separation π[99]:

$$w_p(r_p) = 2 \int_0^{\pi_{max}} \xi(r_p, \pi)\, d\pi. \tag{1.2}$$

A critical aspect of this analysis is the choice of the integration limit, π_{max}. While a larger π_{max} theoretically captures more of the real-space signal by integrating out velocity effects[100;101], it introduces additional noise from uncorrelated pairs and increases sensitivity to modeling uncertainties[102;103]. Conversely, a π_{max} that is too small fails to fully marginalize over RSD, leading to biased results in the recovery of the Alcock-Paczynski parameters.

While recent literature has explored the galaxy bispectrum multipoles to enhance constraints, the projected correlation function remains a vital tool due to its robustness against non-linear velocity models[104;105]. The geometric distortions mix the transverse and longitudinal scales, which must be accounted for using efficient modeling techniques[106;107].

The geometric distortions arising from an incorrect fiducial cosmology mix the transverse and longitudinal scales, an effect that must be carefully accounted for in the $w_p(r_p)$ analysis[cite: 852]. Following the established methodology for power spectrum and bispectrum analysis[67;94], we examine the stability of these measurements across a range of π_{max} values using the AbacusSummit simulation suite.

In our work, we utilize the DESI-specified Halo Occupation Distribution (HOD) parameters for LRG and QSO samples (Emission Line Galaxies are omitted from our study because of the lack of important statistical data that is arisen due to lack of satellite galaxy populations), alongside the DESI logarithmic binning schemes as established in recent literature[1;108].For a sample of Luminous Red Galaxies (LRGs), the HOD can be accurately described using a standard "vanilla" model originally presented in[109]. This model, often referred to as the vanilla HOD, is defined by:

$$\bar{n}\text{cent}^{\text{LRG}}(M) = \frac{fic}{2}\text{erfc}\left[\frac{\log_{10}(M_{\text{cut}}/M)}{\sqrt{2}\sigma}\right], \tag{1.3}$$

$$\bar{n}\text{sat}^{\text{LRG}}(M) = \left[\frac{M - \kappa M\text{cut}}{M_1}\right]^{\alpha} \bar{n}_{\text{cent}}^{\text{LRG}}(M). \tag{1.4}$$

The five core parameters characterizing this model are M_{cut}, M_1, σ, α, and κ. Specifically, M_{cut} represents the minimum halo mass required to host a central galaxy, while M_1 denotes the approximate halo mass threshold for hosting a single satellite galaxy. The σ parameter determines the sharpness of the transition from zero to one in central galaxy occupancy. The power-law index for satellite galaxies is given by α, and κM_{cut} defines the lower mass bound for satellite habitation. We include a modulation term, $\bar{n}_{\text{cent}}^{\text{LRG}}(M)$, in the satellite function to effectively exclude satellites from haloes that lack a central galaxy. Furthermore, an incompleteness parameter, $f_{\rm ic}$ (where $0 < f_{\rm ic} \le 1$, in our paper it is just equal to 1), acts as a downsampling factor to align the mock galaxy number density with observed clustering measurements.For Quasars (QSOs), we employ a nearly identical HOD framework with one key modification: we omit the central modulation term in the satellite occupation function. This adjustment is based on the lack of evidence suggesting a strong physical association between satellite QSOs and the presence of a central QSO. Consequently, the satellite occupation for QSOs is expressed as:

$$\bar{n}\mathrm{sat}^{\mathrm{QSO}}(M) = \left[\frac{M - \kappa M\mathrm{cut}}{M_1}\right]^{\alpha}. \tag{1.5}$$

All parameters are given in the table below:

Table 1.1: *Priors used for LRG and QSO HOD fits, as adopted from*[1]*. The parameters utilize broad Gaussian priors, $N(\mu, \sigma)$, with additional hard bounds as listed. Mass units are expressed in $h^{-1}M_\odot$.*

Params	LRG		QSO	
	Prior	Bounds	Prior	Bounds
$\log M_{\rm cut}$	$N(13.0, 1.0)$	$[12, 13.8]$	$N(12.7, 1.0)$	$[11.2, 14.0]$
$\log M_1$	$N(14.0, 1.0)$	$[12.5, 15.5]$	$N(15.0, 1.0)$	$[12.0, 16.0]$
σ	$N(0.5, 0.5)$	$[0.0, 3.0]$	$N(0.5, 0.5)$	$[0.0, 3.0]$
α	$N(1.0, 0.5)$	$[0.0, 2.0]$	$N(1.0, 0.5)$	$[0.3, 2.0]$
κ	$N(0.5, 0.5)$	$[0.0, 10.0]$	$N(0.5, 0.5)$	$[0.3, 3.0]$

Chapter 2

Mixing bispectrum multipoles under geometric distortions

In this Chapter, we use the results from the paper that was published in 2024[2].

2.1 Alcock-Paczynski Distortions

The Alcock-Paczynski (AP) distortion parameters are defined as:

$$d_{||} = \alpha_{||} d^{\mathrm{t}}_{||}, \tag{2.1}$$

$$d_{\perp} = \alpha_{\perp} d^{\mathrm{t}}_{\perp}. \tag{2.2}$$

These parameters link the cosmological model to observable quantities via:

$$\alpha_{||} = \frac{H^{\mathrm{t}}(z)}{H^{\mathrm{fid}}(z)}, \tag{2.3}$$

$$\alpha_{\perp} = \frac{D_A^{\mathrm{fid}}(z)}{D_A^{\mathrm{t}}(z)}, \tag{2.4}$$

where $H(z)$ represents the Hubble parameter and $D_A(z)$ denotes the angular diameter distance at a given redshift z. These spatial distortions correspond to dual distortions in Fourier space:

$$k_{||}^{\mathrm{t}} = \alpha_{||} k_{||}, \tag{2.5}$$

$$k_{\perp}^{\mathrm{t}} = \alpha_{\perp} k_{\perp}. \tag{2.6}$$

In this analysis, we utilize the following parameters:

$$\alpha_V = \sqrt[3]{\alpha_{\perp}^2 \alpha_{||}}, \tag{2.7}$$

$$\alpha_\epsilon = \sqrt[3]{\frac{\alpha_{||}^2}{\alpha_{\perp}^2}}. \tag{2.8}$$

While the definition of α_V is standard within the field[110], our characterization of α_ϵ varies from the traditional $\epsilon = \sqrt[3]{\alpha_{||}/\alpha_{\perp}} - 1$. Although both α_ϵ and ϵ can be used without loss of information, we demonstrate that the definition in Eq. (2.8) provides a more intuitive geometric interpretation. To linear order, these two sets of parameters relate as follows:

$$\delta\alpha_V = \frac{1}{3}\left(\delta\alpha_{||} + 2\delta\alpha_{\perp}\right), \tag{2.9}$$

$$\delta\alpha_\epsilon = \frac{2}{3}(\delta\alpha_{||} - \delta\alpha_{\perp}). \tag{2.10}$$

The length of every wavevector and its angle relative to the LOS axis transform according to:

$$\begin{aligned} k^{\mathrm{t}} &= k\sqrt{\mu^2(\alpha_{||}^2 - \alpha_{\perp}^2) + \alpha_{\perp}^2} \\ &= k\alpha_V \sqrt{\mu^2(\alpha_\epsilon^2 - 1/\alpha_\epsilon) + 1/\alpha_\epsilon}, \end{aligned} \tag{2.11}$$

$$\begin{aligned} \mu^t &= \mu \frac{\alpha_{||}}{\sqrt{\mu^2(\alpha_{||}^2 - \alpha_{\perp}^2) + \alpha_{\perp}^2}} \\ &= \mu \frac{\alpha_\epsilon}{\sqrt{\mu^2(\alpha_\epsilon^2 - 1/\alpha_\epsilon) + 1/\alpha_\epsilon}}. \end{aligned} \tag{2.12}$$

Approximated to the linear order in AP parameters, these transformations simplify to:

$$k^{\rm t} = k\left[1 + \delta\alpha_V + L_2(\mu)\delta\alpha_\epsilon\right], \tag{2.13}$$

$$\mu^{\rm t} = \mu\left[1 + \frac{3}{2}(1-\mu^2)\delta\alpha_\epsilon\right]. \tag{2.14}$$

Here, α_V represents the mean relative distortion of wavevector lengths across all directions, while α_ϵ signifies the magnitude of the dipole distortion relative to the LOS. Notably, the wavevector angle is influenced solely by α_ϵ. This clear geometric significance motivated the adoption of the parameters defined in Eqs. (2.7)-(2.8).

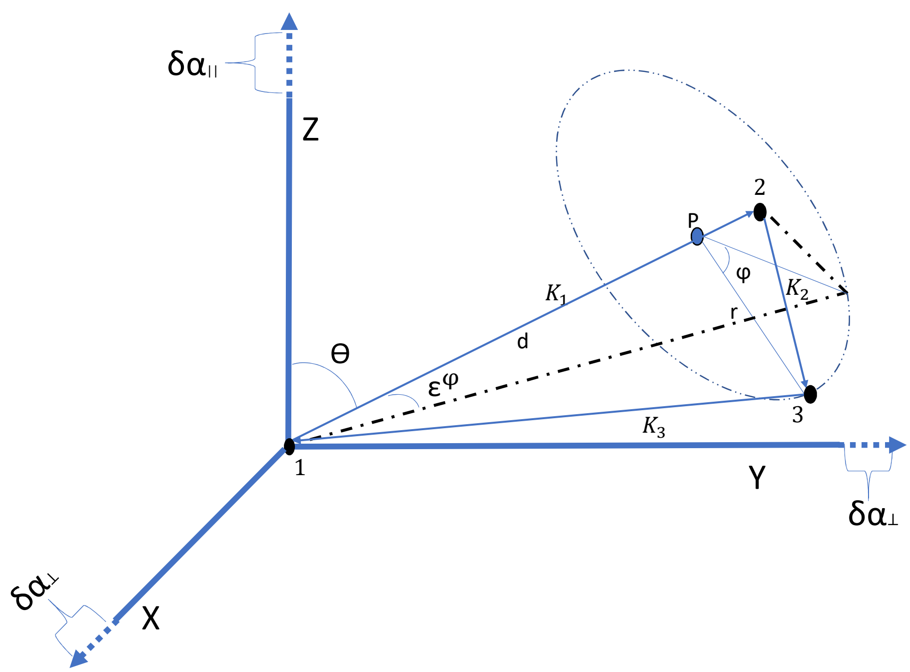

Figure 2.1: *Depiction of the three wavevectors defining a bispectrum and the associated geometry. Points 1 and 2 are situated in the y-z plane.*

The bispectrum is determined by three wavevectors constrained by $\mathbf{k}_1 + \mathbf{k}_2 + \mathbf{k}_3 = 0$, typically visualized as a triangle. Its value depends on the wavevector lengths (k_1, k_2, k_3) and their orientation relative to the LOS, parametrized by μ_1 (the cosine of $\mathbf{k}_1$ with the LOS) and ϕ (the triangle's rotation angle from the y-z plane).

To apply these distortion formulae, we express the cosine and sine of these wavevectors using the five base parameters:

$$\mu_1 = \mu_\theta, \tag{2.15}$$

$$\mu_2 = -\mu_{12}\mu_\theta + \mu_\phi \nu_{12}\nu_\theta, \tag{2.16}$$

$$\mu_3 = -\mu_{31}\mu_\theta - \mu_\phi \nu_{31}\nu_\theta, \tag{2.17}$$

where subscripts 12 and 31 denote angles between wavevectors $\mathbf{k}_1$, $\mathbf{k}_2$, and $\mathbf{k}_3$, $\mathbf{k}_1$ respectively:

$$\mu_{12} = \frac{\mathbf{k}_1 \cdot \mathbf{k}_2}{k_1 k_2}, \quad \mu_{31} = \frac{\mathbf{k}_3 \cdot \mathbf{k}_1}{k_3 k_1}. \tag{2.18}$$

While μ_1 is a primary parameter, μ_2 and μ_3 are derived in Appendix A.1. Changes to the angle ϕ due to distortions are subdominant and thus omitted from our multipole computations.

Furthermore, AP distortions rescale all volumes by $1/\alpha_V^3$, resulting in a wavenumber-independent amplitude shift. This rescales the power spectrum by $1/\alpha_V^3$ and the bispectrum by $1/\alpha_V^6$, which in linear approximation corresponds to factors of $1 - 3\delta\alpha_V$ and $1 - 6\delta\alpha_V$. Since this rescaling is mathematically trivial, it should be modeled exactly, even when shape distortions use linear approximations. We do not include this global factor in the subsequent formulae.

2.2 Distortions of the Power and Bispectrum

The power spectrum is fundamentally a function of wavenumber length and its orientation relative to the line-of-sight (LOS). It is conventionally expanded using Legendre moments as follows[cite: 1615]:

$$P(k,\mu) = \sum_l P_l(k) L_l(\mu). \tag{2.19}$$

These moments are computed through the following integral:

$$P_l(k) = \frac{2l+1}{2} \int \mathrm{d}\mu \; P(k,\mu) L_l(\mu). \tag{2.20}$$

Alcock-Paczynski (AP) distortions warped the measured power spectrum relative to the true spectrum, P^{t}, according to the relation:

$$P(k,\mu) = P^{\mathrm{t}}\left(k^{\mathrm{t}}\left[k,\mu\right], \mu^{\mathrm{t}}\left[k,\mu\right]\right). \tag{2.21}$$

To linear order, the relationship between measured and true multipoles can be expressed as:

$$\begin{aligned} P = P^{\mathrm{t}} &+ \frac{\partial P^{\mathrm{t}}}{\partial k}\left(\frac{\partial k}{\partial \alpha_V}\delta\alpha_V + \frac{\partial k}{\partial \alpha_\epsilon}\delta\alpha_\epsilon\right) + \\ &+ \frac{\partial P^{\mathrm{t}}}{\partial \mu}\left(\frac{\partial \mu}{\partial \alpha_V}\delta\alpha_V + \frac{\partial \mu}{\partial \alpha_\epsilon}\delta\alpha_\epsilon\right). \end{aligned} \tag{2.22}$$

Applying the transformations for k and μ, this becomes:

$$P = P^{\mathrm{t}} + \frac{\partial P^{\mathrm{t}}}{\partial \ln k}\delta\alpha_V + \frac{\partial P^{\mathrm{t}}}{\partial \ln k} L_2(\mu)\delta\alpha_\epsilon + \frac{\partial P^{\mathrm{t}}}{\partial \ln \mu}\frac{3}{2}(1-\mu^2)\delta\alpha_\epsilon. \tag{2.23}$$

For the specific multipoles, the expansion yields:

$$\begin{aligned} P_\ell = \frac{2l+1}{2} \sum_{\ell'} \int \mathrm{d}\mu \Bigg[& P^{\mathrm{t}}_{\ell'} L_{\ell'}(\mu) + \frac{\partial P^{\mathrm{t}}_{\ell'}}{\partial \ln k} L_{\ell'}(\mu)\delta\alpha_V + \\ + & \frac{\partial P^{\mathrm{t}}_{\ell'}}{\partial \ln k} L_{\ell'}(\mu) L_2(\mu)\delta\alpha_\epsilon + P^{\mathrm{t}}_{\ell'}\frac{\partial L_{\ell'}(\mu)}{\partial \ln \mu}\frac{3}{2}(1-\mu^2)\delta\alpha_\epsilon \Bigg] L_\ell(\mu), \end{aligned} \tag{2.24}$$

which results in the final form:

$$P_\ell = P^{\rm t}_\ell + \frac{\partial P^{\rm t}_\ell}{\partial \ln k}\delta\alpha_V + \sum_{l'} \frac{\partial P^{\rm t}_{\ell'}}{\partial \ln k} A_{ll'}\delta\alpha_\epsilon + \sum_{l'} P^{\rm t}_{l'} B_{ll'}\delta\alpha_\epsilon.$$

$$A_{ll'} = \frac{2\ell+1}{2}\int \mathrm{d}\mu\; L_{\ell'}(\mu)L_\ell(\mu)L_2(\mu), \tag{2.25}$$

$$B_{ll'} = \frac{2\ell+1}{2}\int \mathrm{d}\mu\; \frac{\partial L_{\ell'}(\mu)}{\partial \ln \mu} L_\ell(\mu)\frac{3}{2}(1-\mu^2). \tag{2.26}$$

The primary term represents a scaling of each multipole by $\delta\alpha_V$. The subsequent terms involve the mixing of different multipoles and are solely dependent on $\delta\alpha_\epsilon$. The analytical mixing coefficients for the first four multipoles are provided in Table 2.1. Note that these coefficients differ by a factor of two from those in Padmanabhan and White [94] due to our use of α_ϵ instead of ϵ.

Table 2.1: *Nonzero mixing coefficients for power spectrum multipoles up to the fourth degree.*

ℓ	ℓ'	$A_{\ell\ell'}$	$B_{\ell\ell'}$
0	2	1/5	3/5
2	0	1	0
2	2	2/7	3/7
2	4	2/7	10/7
4	2	18/35	−36/35
4	4	20/77	30/77

2.2.1 Geometric Distortions of the Bispectrum

The galaxy bispectrum is a function of five parameters and is typically expanded in spherical multipoles as:

$$B(k_1,k_2,k_3,\mu,\phi) = \sum_{\ell m} B_{\ell m}(k_1,k_2,k_3)Y_{\ell m}(\theta_1,\phi), \tag{2.27}$$

where $\theta_1 = \arccos(\mu_1)$. The corresponding multipoles are calculated via[cite: 1721]:

$$B_{\ell m}(k_1,k_2,k_3) = \int \mathrm{d}\mu_1 \mathrm{d}\phi\; B(k_1,k_2,k_3,\mu_1,\phi)Y_{\ell m}(\theta_1,\phi). \tag{2.28}$$

As multipoles with $m \neq 0$ exhibit negligible amplitudes, we focus exclusively on the primary index for the remainder of this analysis. Measured and true bispectra are linked through the following relation:

$$B(k_1, k_2, k_3, \mu_1, \phi) = B^{\rm t}(k_1^{\rm t}, k_2^{\rm t}, k_3^{\rm t}, \mu_1^{\rm t}, \phi^{\rm t}). \tag{2.29}$$

To linear order, and neglecting subdominant ϕ-derivatives, the distortions are given by:

$$B = B^{\rm t} + \sum_{i=1,2,3} \frac{\partial B^{\rm t}}{\partial \ln k_i}\delta\alpha_V + \sum_{i=1,2,3} \frac{\partial B^{\rm t}}{\partial \ln k_i} L_2(\mu_i)\delta\alpha_\epsilon + \frac{\partial B^{\rm t}}{\partial \ln \mu_1}\frac{3}{2}(1-\mu_1^2)\delta\alpha_\epsilon. \tag{2.30}$$

Decomposing this into multipoles results in:

$$B_\ell = B_\ell^{\rm t} + \sum_{i=1}^{3} \frac{\partial B_\ell^{\rm t}}{\partial \ln k_i}\delta\alpha_V + \sum_{\ell', m',} \sum_{i=1}^{3} \frac{\partial B_{\ell' m'}^{\rm t}}{\partial \ln k_i} C_{\ell\ell' m'}^{(i)}\delta\alpha_\epsilon + \sum_{\ell'} \frac{\partial B_{\ell'}^{\rm t}}{\partial \ln \mu_1} D_{\ell\ell'}\delta\alpha_\epsilon, \tag{2.31}$$

where the mixing coefficients are defined by:

$$C_{\ell\ell' m'}^{(i)} = \int {\rm d}\mu_1 {\rm d}\phi \; L_2(\mu_i) Y_{\ell 0}(\mu_1) Y_{\ell' m'}(\mu_1) \tag{2.32}$$

$$D_{\ell\ell'} = \frac{3}{2}\int {\rm d}\mu_1 {\rm d}\phi \; \frac{\partial Y_{\ell' 0}(\mu_1)}{\partial \ln \mu_1}(1-\mu_1^2) Y_{\ell 0}(\mu_1) \tag{2.33}$$

These analytical coefficients are summarized in Tables 2.2 and 2.3.

2.3 Testing Linear Approximation

To evaluate the validity of the derived linear expansions in Eq.-(2.26) and Eqs. (2.31)-(2.33), we perform numerical tests using linear theory within the standard ΛCDM framework (detailed in Appendix). We adopt the best-fit cosmological parameters as determined by the `Planck` satellite mission[111].

The validation process begins by computing the power spectrum using the exact distortion formula in Eq. (2.21), which is then compared against the linear approximations. Figure 2.2

Table 2.2: *All nonzero coefficients $C^{(i)}_{\ell\ell'm'}$ up to $\ell = 4$.*

ℓ	ℓ'	m'	$C^{(1)}_{\ell\ell'm'}$	$C^{(2)}_{\ell\ell'm'}$	$C^{(3)}_{\ell\ell'm'}$
0	2	0	$1/\sqrt{5}$	$L_2(\mu_{12})/\sqrt{5}$	$L_2(\mu_{31})/\sqrt{5}$
0	2	2	0	$\frac{1}{2}\sqrt{3/10}(1-\mu_{12}^2)$	$\frac{1}{2}\sqrt{3/10}(1-\mu_{31}^2)$
2	0	0	$1/\sqrt{5}$	$L_2(\mu_{12})/2\sqrt{5}$	$L_2(\mu_{31})/2\sqrt{5}$
2	2	0	$2/7$	$2L_2(\mu_{12})/7$	$2L_2(\mu_{31})/7$
2	2	2	0	$-\frac{1}{7}\sqrt{3/2}(1-\mu_{12}^2)$	$-\frac{1}{7}\sqrt{3/2}(1-\mu_{31}^2)$
2	4	0	$6/7\sqrt{5}$	$6L_2(\mu_{12})/7\sqrt{5}$	$6L_2(\mu_{31})/7\sqrt{5}$
2	4	2	0	$\frac{3}{14\sqrt{2}}(1-\mu_{12}^2)$	$\frac{3}{14\sqrt{2}}(1-\mu_{31}^2)$
4	2	0	$6/7\sqrt{5}$	$6L_2(\mu_{12})/7\sqrt{5}$	$6L_2(\mu_{31})/7\sqrt{5}$
4	2	2	0	$\frac{1}{14}\sqrt{3/10}(1-\mu_{12}^2)$	$\frac{1}{14}\sqrt{3/10}(1-\mu_{31}^2)$
4	4	0	$20/77$	$20L_2(\mu_{12})/77$	$20L_2(\mu_{31})/77$
4	4	2	0	$-\frac{9}{77}\sqrt{5/2}(1-\mu_{12}^2)$	$-\frac{9}{77}\sqrt{5/2}(1-\mu_{31}^2)$
4	6	0	$15/11\sqrt{13}$	$15L_2(\mu_{12})/11\sqrt{13}$	$15L_2(\mu_{31})/11\sqrt{13}$
4	6	2	0	$\frac{1}{22}\sqrt{105/13}(1-\mu_{12}^2)$	$\frac{1}{22}\sqrt{105/13}(1-\mu_{31}^2)$

Table 2.3: *All nonzero $D_{\ell\ell'}$ coefficients up to $\ell = 4$.*

ℓ	ℓ'	$D_{\ell\ell'}$
0	2	$3/\sqrt{5}$
2	2	$3/7$
2	4	$6/7\sqrt{5}$
4	2	$-12/7\sqrt{5}$
4	4	$30/77$
4	6	$105/11\sqrt{13}$

illustrates the ratio of these computations to the undistorted (fiducial) power spectrum. For these tests, we assume a 1% offset in both α_V and α_ϵ; as expected, the accuracy of the linear approximation improves as the offset decreases.

Figure 2.2 highlights the first three even multipoles within the range $0 < k < 0.2h^{-1}$ Mpc. It is evident that α_V exerts a more significant influence on the monopole than α_ϵ. Specifically, a 1% deviation in α_V induces a roughly 2% shift in monopole amplitude, featuring a distinct Baryon Acoustic Oscillation (BAO) signature. The linear approximation demonstrates excellent agreement with exact results here. In the quadrupole, α_V distortions are smaller but remain non-negligible, contributing a 2% offset compared to the 6% offset driven by α_ϵ. The quadrupole is predominantly sensitive to α_ϵ, where a 1% offset can lead to amplitude shifts of up to 30%. Overall, the linear model performs remarkably well across all three power spectrum multipoles.

The corresponding analysis for the bispectrum is shown in Figure 2.3. The bispectrum monopole is almost entirely governed by α_V distortions, where a 1% shift results in a 4% amplitude change with a pronounced BAO feature. For the bispectrum quadrupole, both α_V and α_ϵ have comparable effects. While the linear approximation remains highly accurate for the monopole, we observe slight deviations in the quadrupole at low wavevectors (k). These deviations primarily affect the amplitude while preserving the BAO peak positions and are most noticeable at small wavenumbers where relative α_ϵ distortions are most impactful.

In contrast, the bispectrum hexadecapole is exceptionally sensitive to α_ϵ distortions. In this case, the linear expansion fails to accurately capture the signal even for minimal distortions. As demonstrated in Figure 2.4, a mere 1% distortion can cause the hexadecapole amplitude to shift by a factor of two, indicating a breakdown of the linear regime for this specific moment.

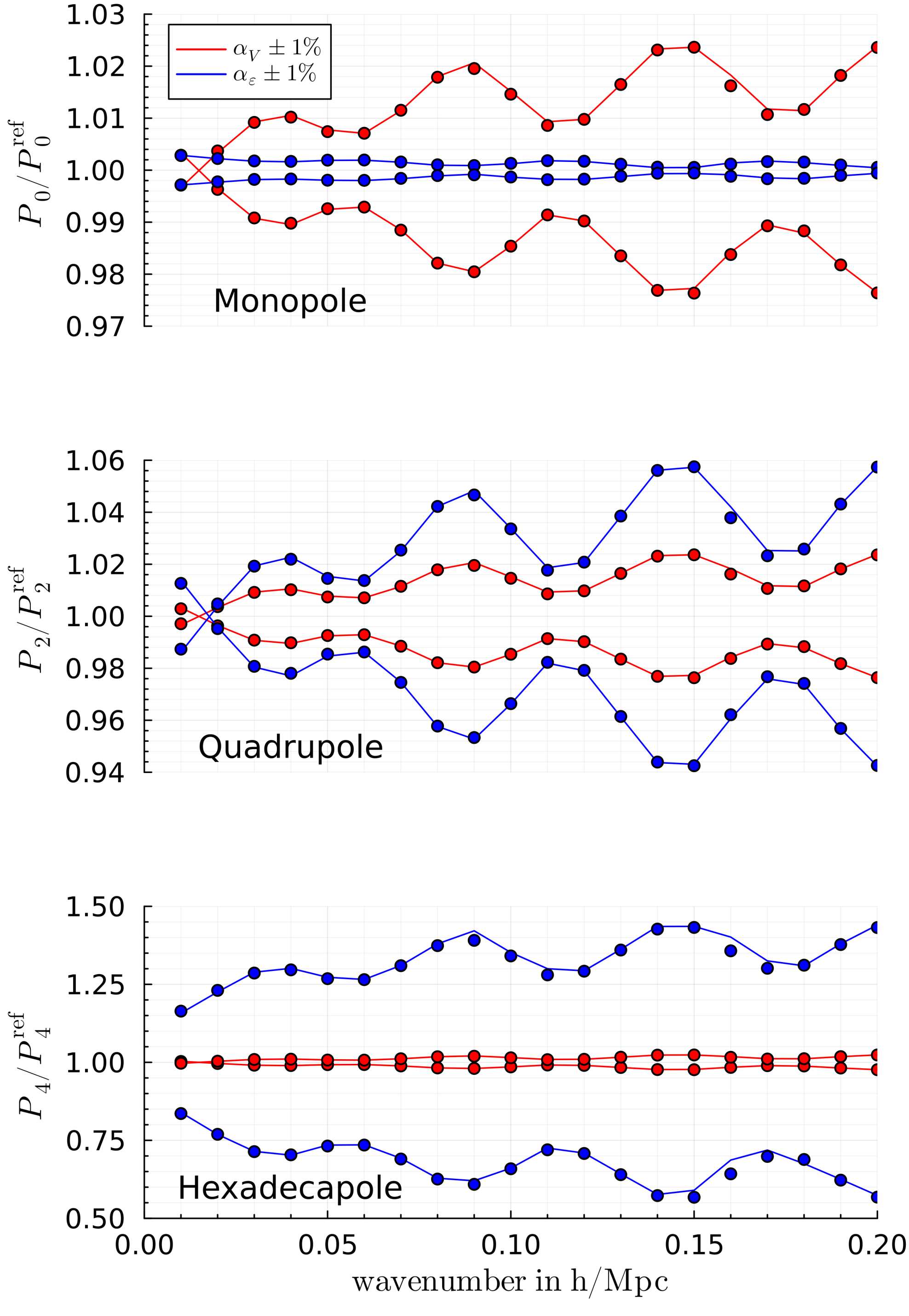

Figure 2.2: *Ratio of distorted power spectrum multipoles to the fiducial ones. Data points represent exact results, while solid lines denote the linear approximation. Panels display the monopole, quadrupole, and hexadecapole from top to bottom. Red markers/lines indicate a 1% α_V offset, and blue markers/lines indicate a 1% α_ϵ offset.*

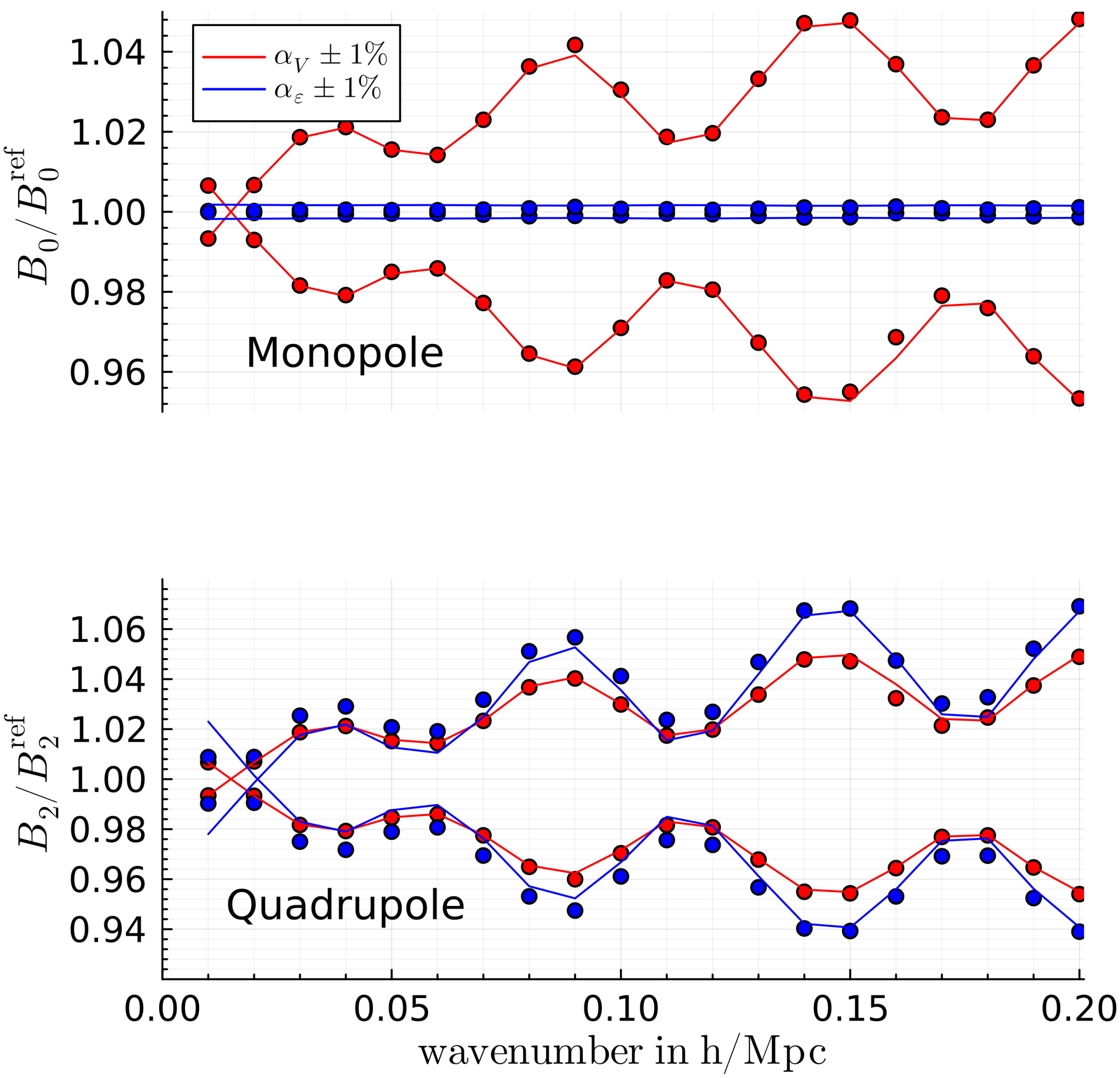

Figure 2.3: *Ratio of distorted bispectrum multipoles to the fiducial ones. Monopole and quadrupole results are shown from top to bottom. Red and blue indicate 1% offsets in α_V and α_ϵ, respectively.*

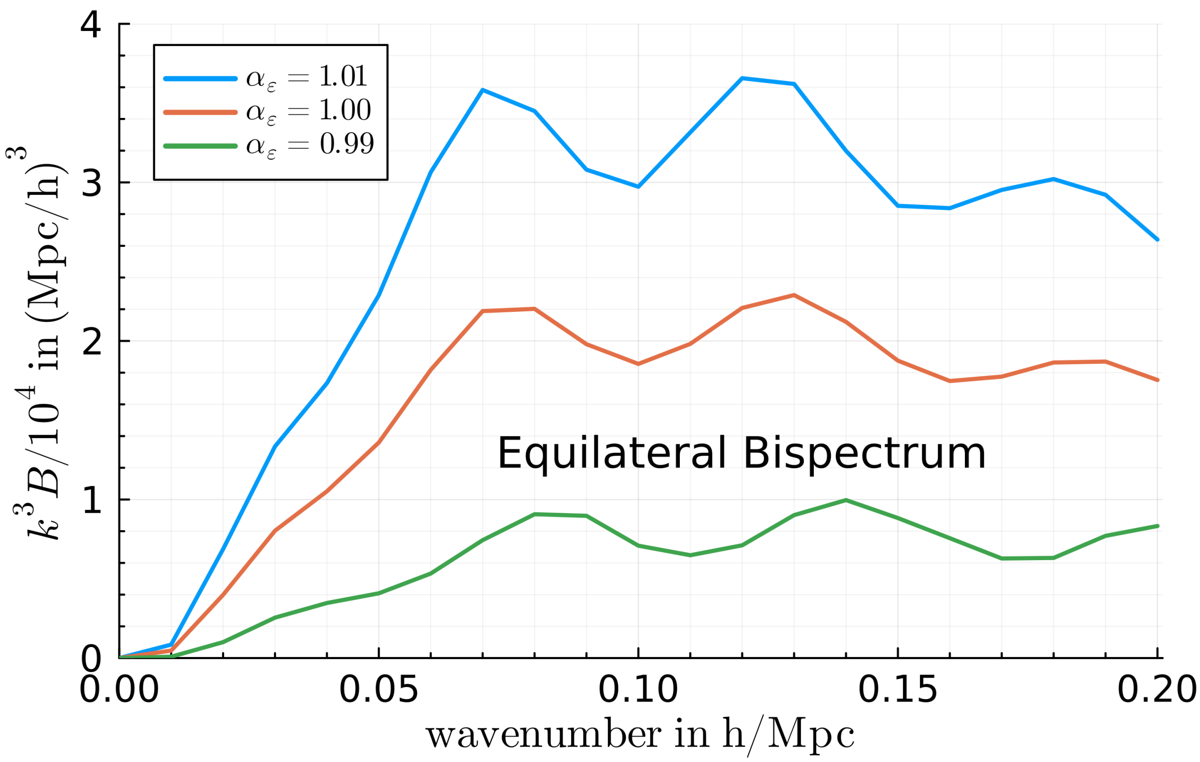

Figure 2.4: *Response of the equilateral bispectrum hexadecapole to a 1% offset in* α_ϵ.

Chapter 3

Optimized Projected Correlation Function

In the second part of this work, we investigate the optimal choice of the integration limit, $\pi_{\rm max}$, for the projected correlation function. Our primary objective is to determine the specific $\pi_{\rm max}$ threshold that maximizes sensitivity toward HOD parametrization and enhances the ability to distinguish between competing cosmological models.

Regarding cosmological sensitivity, our findings align with theoretical expectations: as the value of $\pi_{\rm max}$ increases, the resulting increase in averaging over line-of-sight separations tends to suppress the signal, thereby reducing sensitivity to variations in the underlying cosmology. Conversely, when focusing on HOD discrimination and the maximization of total Fisher information, we find that the optimal integration limit is not constant. Instead, the most effective $\pi_{\rm max}$ varies significantly depending on the specific galaxy sample characteristics and on the various parameters.

3.1 Optimized π_{max} for HOD parametrization

Firstly, we use Abacussummit simulations of small boxes (in total 1824),

We have approximately 1800 small boxes, with 14 radial bins in total, and that gives us

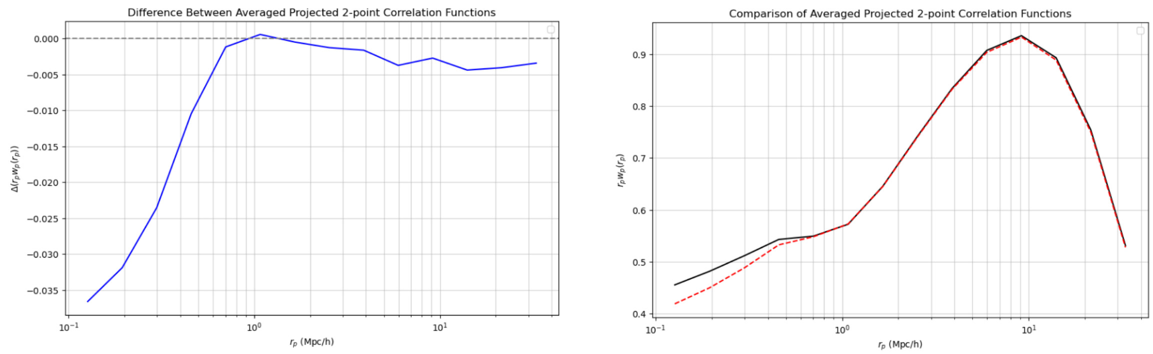

Figure 3.1: *the difference of the projected correlation function times distance bin for slight perturbation of LRG parameter, Mcut, using the AbacusSummit* `c000` *(Base Planck) cosmology. This analysis examines the sensitivity of the projected correlation function $w_p(r_p)$ for given $\pi_{max} = 100$.*

the opportunity to use Fisher information and covariance matrix statistics. The Fisher Information Matrix (FIM) provides a rigorous mathematical framework for predicting how well a set of parameters can be constrained by a specific observable. In the context of large-scale structure analysis, the Fisher matrix effectively quantifies the sensitivity of the projected correlation function, $w_p(r_p)$, to variations in the underlying Halo Occupation Distribution (HOD) and cosmological parameters.

The Fisher Matrix F_{ij} is defined as the expectation value of the second derivative of the log-likelihood function with respect to the parameters θ_i and θ_j:

$$F_{ij} = -\left\langle \frac{\partial^2 \ln \mathcal{L}}{\partial\theta_i \partial\theta_j} \right\rangle, \tag{3.1}$$

where $\ln \mathcal{L}$ is the log-likelihood of the data given the model parameters $\boldsymbol{\theta}$. Under the standard assumption of a Gaussian likelihood where the covariance matrix $\mathbf{C}$ is assumed to be independent of the parameters, the Fisher Matrix simplifies to:

$$F_{ij} = \sum_{m,n} \frac{\partial y_m}{\partial \theta_i} [C^{-1}]_{m,n} \frac{\partial y_n}{\partial \theta_j}. \tag{3.2}$$

$$\sigma_{\theta_i} \geq \sqrt{(F^{-1})_{ii}}. \tag{3.3}$$

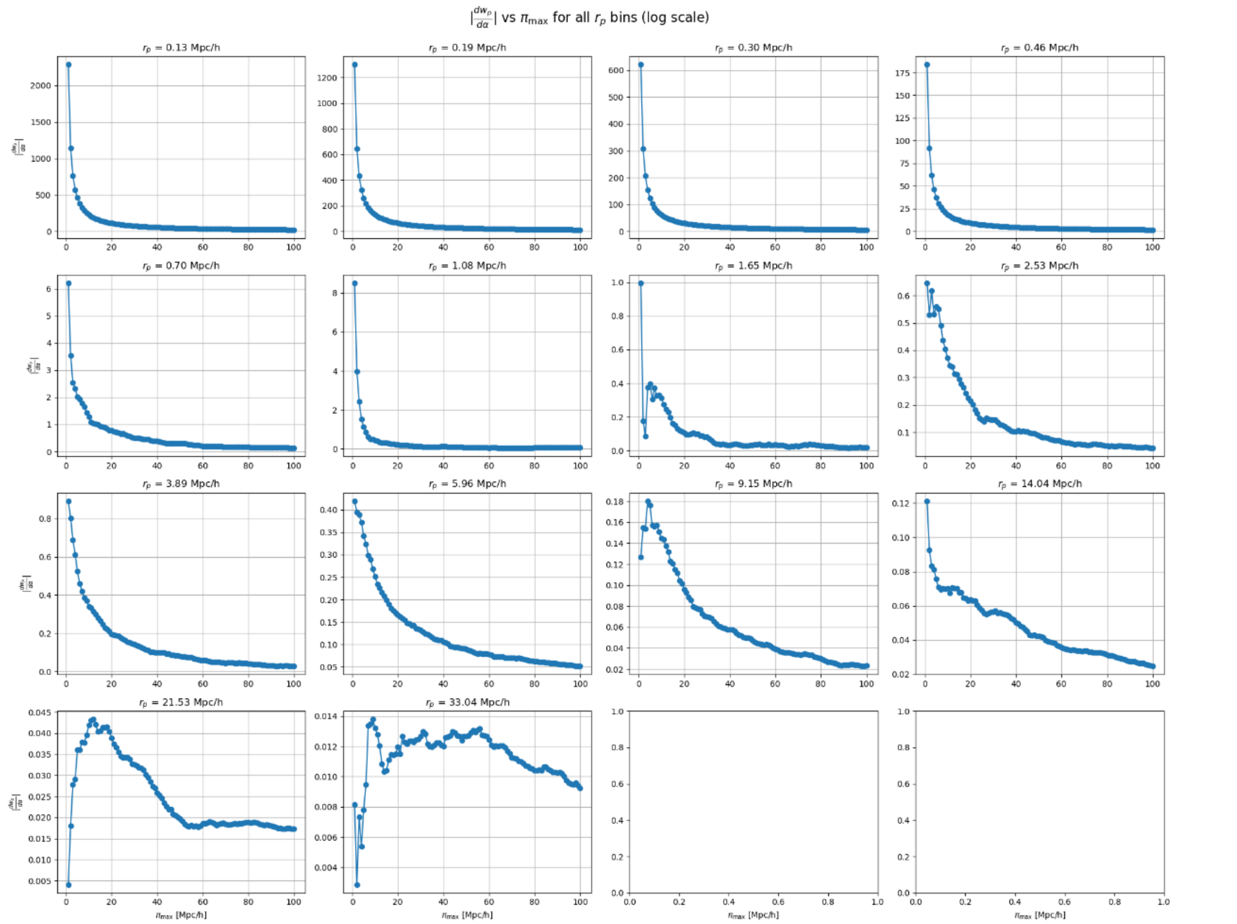

Figure 3.2: *Projected Correlation function derivatives for different bins. For σ HOD parameter for LRG-s.*

In this expression, $\mathbf{y}$ is the model vector (e.g., the predicted w_p values in specific distance bins). In our studies, we use Fisher information like quantities for the sake of simplicity and convenience as depicted below and also in the Figures. $\mathbf{C}$ is the covariance matrix. The covariance matrix accounts for the statistical uncertainties, including shot noise and cosmic variance, and is defined as:

$$C_{mn} = \langle (y_m - \bar{y}_m)(y_n - \bar{y}_n) \rangle. \tag{3.4}$$

The precision with which we can measure a parameter is limited by the Cramer-Rao bound, which states that the variance of an unbiased estimator is at least the inverse of the

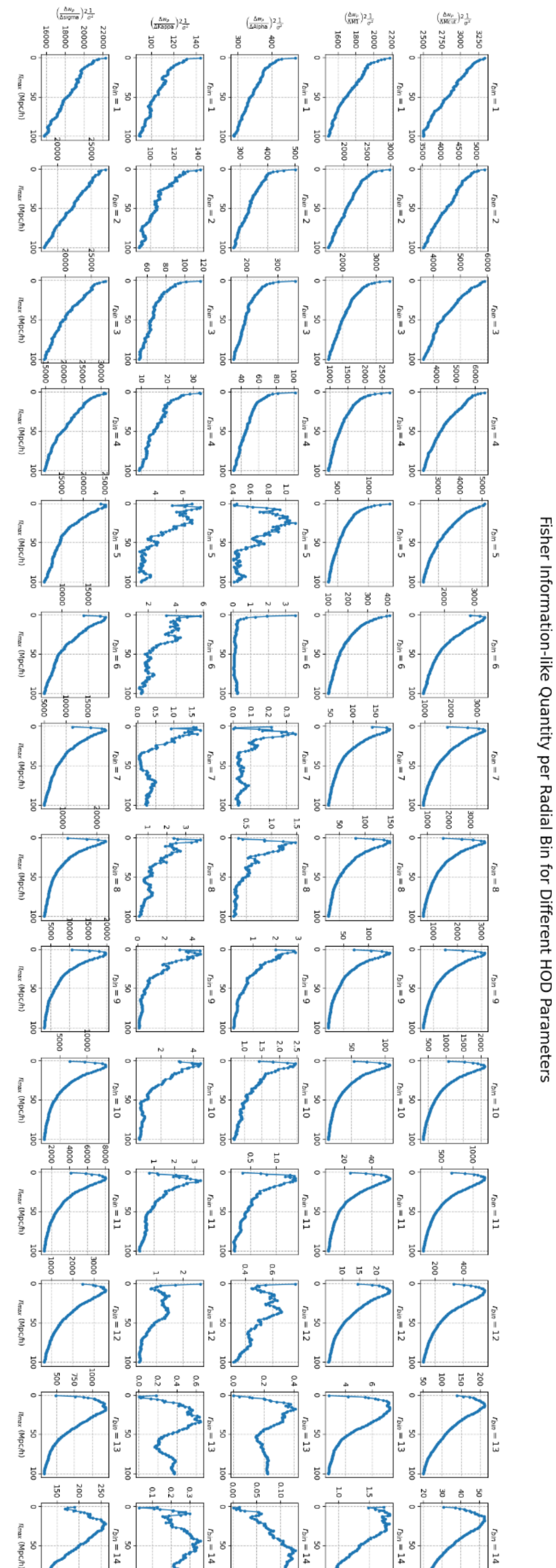

Figure 3.3: *Fisher information like quantity for each HOD parameter, and for seperate radial bins.*

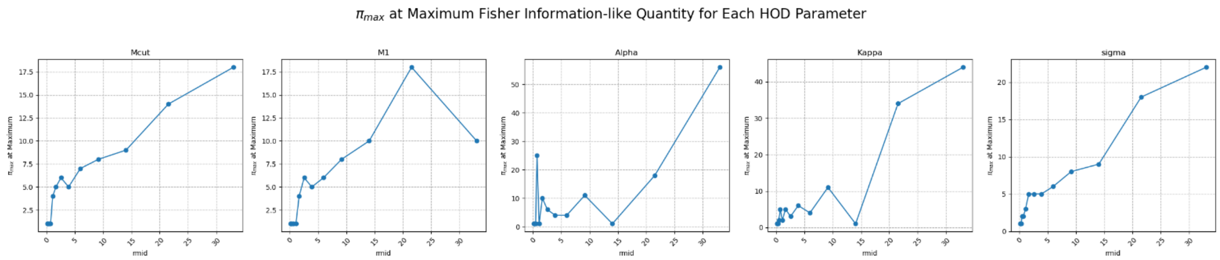

Figure 3.4: *π_{max} maximum vs r_{bin} for each HOD parameter. Here, it is visible that for satellite parameters κ and α, results are noisy, which is due to their small sensitivity towards the total galaxy population.*

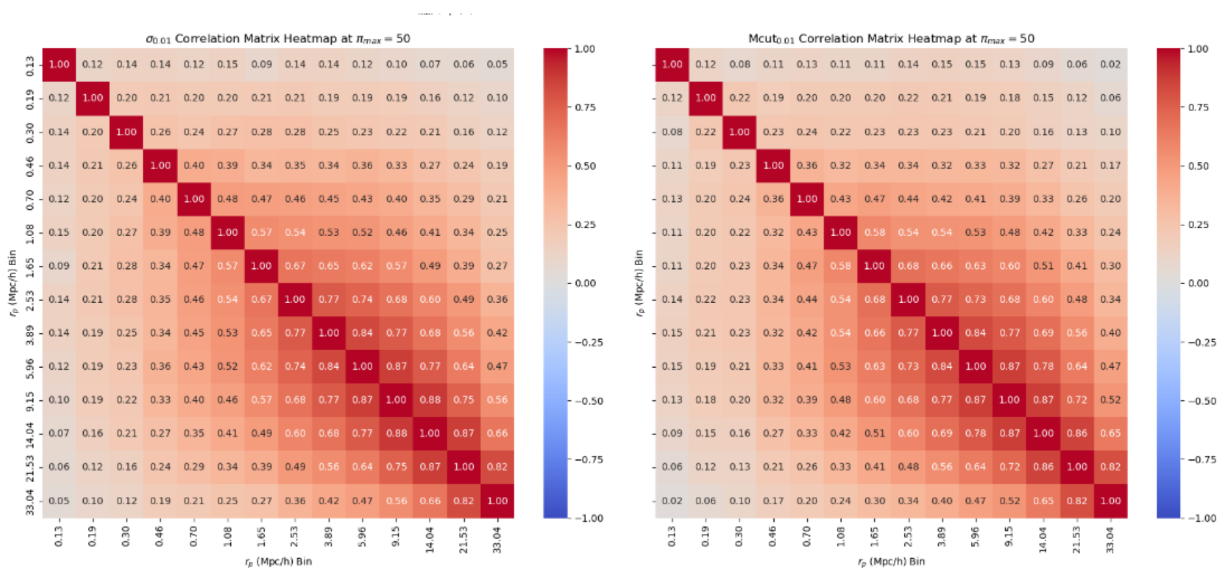

Figure 3.5: *The two Correlation Matrix graphs are for fixed $\pi_{max} = 50$, resulting from varying M_{cut} and σ HOD parameters*

Fisher information. The marginalized 1σ uncertainty on a parameter θ_i is given by:

In our analysis, we utilize finite-difference methods to compute the derivatives in Eq. (3.2) by applying slight perturbations to the LRG and QSO and cosmological parameters within the AbacusSummit `c000` simulation suite. This allows us to quantify the information content as a function of the line-of-sight integration limit π_{max}. More precisely, we use the Fisher information like quantity (FILQ):

$$FILQ = \left(\frac{\Delta w_p}{\Delta \mathrm{HOD}}\right)^2 \frac{1}{\sigma^2} \tag{3.5}$$

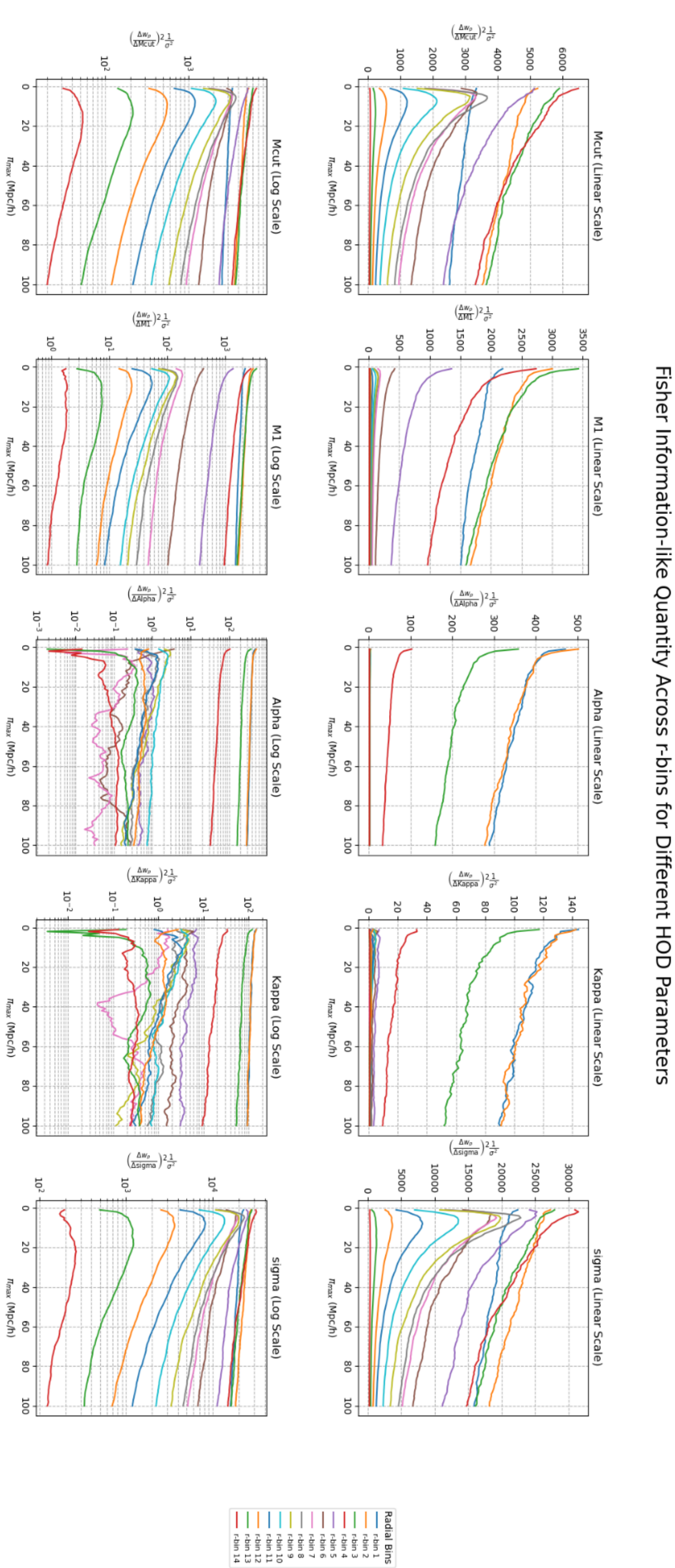

Figure 3.6: *Final results of LRG small boxes*

To plot and find optimal π_{max} values. For small boxes, the noisy part is the derivatives, as each small box volume is 64 times smaller than a large box, and even averaging over 1800 boxes does not improve in dissipating the noise. However, σ is much smoother as it is computed from the covariance matrix.

The main result of this analysis is in Fig. 3.4, where it is clearly observed that the optimal π_{max} varies approximately linearly according to radial bin. This can be said with definite certainty about M_{cut} and σ, the trend is clear with M_1 (although at very low and very high distances noise becomes more dominant), however for satellite parameters α and κ the results are stochastic as expected (varying each of these two parameters very slightly changes the total galaxy population).

3.2 Optimization in Large Box Simulations

On contrary to small boxes, in FILQ, the derivative part is much smoother, but errors are calculated straightforwardly with standard deviation from the 25 large boxes, and thus are noisy.

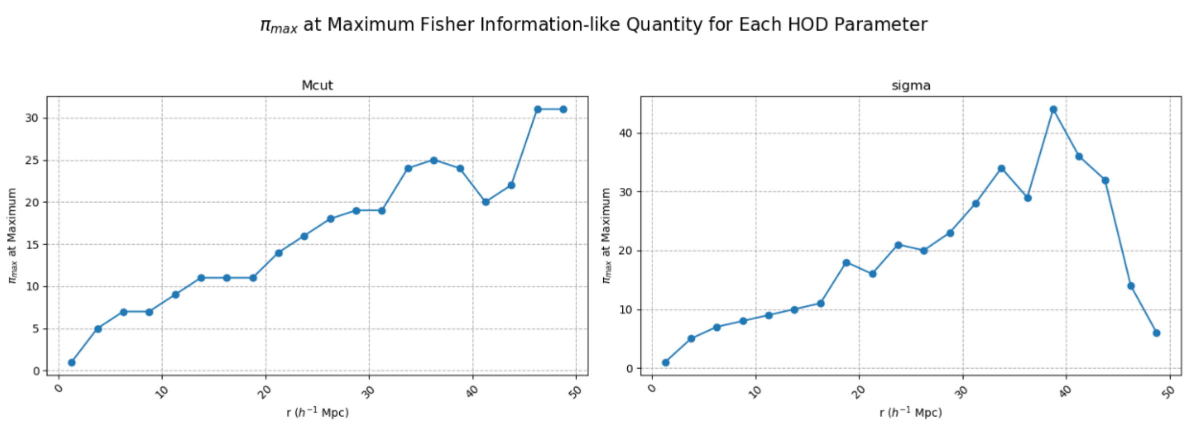

Figure 3.7: *Fisher information like quantity analysis for large boxes. Only final results for π_{max} optimization are displayed. A clear linear dependence is observed with M_{cut} and with σ, the signal becomes noisy for higher radial bins*

3.3 HOD Parameter Optimization for Cosmological Minimal Deviance

To investigate the degeneracy between galaxy assembly bias and cosmological parameters, we perform an optimization routine to determine the best-fit HOD parameters for various `AbacusSummit` cosmologies. The objective of this optimization is to minimize the difference between the clustering signal of a given cosmology and the base `Planck` (`c000`) results, assuming a fixed integration limit of $\pi_{\rm max} = 100\,h^{-1}$Mpc. Table 3.1 summarizes the resulting HOD parameters for each tested cosmological box. Additionally, varying $\pi_{\rm max}$ does not give any peculiar results, simply in the case of different cosmologies, the more averaging (thus higher $\pi_{\rm max}$) is better. In order to get the results in Table 3.1, initially, we performed only 2-dimensional grid analysis (for M_{cut} and σ, since these two are the most sensitive), after that the bestfit value for M_1 was found, and then again 2-dimensional grid analysis for the satellite parameters, α and κ.

Table 3.1: *Optimized HOD parameters for different AbacusSummit cosmologies to minimize clustering differences relative to the base Planck cosmology (`c000`) at $\pi_{max} = 100\,h^{-1}$Mpc.*

Cosmology	$\log M_{\rm cut}$	σ	$\log M_1$	α	κ
C000 (Base Planck)	12.70	0.17	13.94	1.07	0.55
C100 ($\omega_b + 2\%$)	12.74	0.17	13.91	1.01	0.60
C102 ($\omega_c + 3.3\%$)	12.72	0.16	13.98	1.08	0.52
C104 ($n_s + 0.01$)	12.82	0.18	13.92	1.07	0.54
C106 ($n_{\rm run} + 0.02$)	12.69	0.17	13.91	1.05	0.57
C108 ($w_0 + 0.1$)	12.73	0.17	13.99	1.09	0.51
C110 ($w_a + 0.1$)	12.80	0.19	13.95	1.07	0.55
C112 ($\sigma_8 + 2\%$)	12.65	0.17	13.84	1.08	0.53
C114 (Mixed Parameters)	12.68	0.20	13.92	1.05	0.56
C117 ($\omega_c + 0.83\%$)	12.81	0.19	13.92	1.02	0.53

Chapter 4

Conclusions

In the first part of this thesis, we derived explicit analytic expressions for the mixing coefficients of bispectrum multipoles to the linear order in Alcock-Paczynski (AP) distortions. These coefficients, presented in Tables 2.2 and 2.3 for multipoles up to $\ell = 4$, are formulated for the standard definition of bispectrum multipoles. However, they can be readily extended to alternative parametrizations, such as those proposed by Sugiyama et al.[52].Our analysis demonstrates that the linear-order mixing coefficients perform remarkably well for all power spectrum multipoles (see Figure 2.2). For the bispectrum, we found that the leading-order mixing model is highly effective for the monopole. Specifically, isotropic stretching (characterized by non-zero α_V) is modeled with high accuracy across all multipoles using the linear expression.Conversely, the linear mixing model is less robust when accounting for anisotropic stretching (non-zero α_ϵ), as illustrated in Figure 2.3. We observed that predictions for the bispectrum quadrupole begin to deviate by a fraction of a percent even at small distortions ($\alpha_\epsilon \sim 1\%$). More notably, even these minor α_ϵ offsets induce substantial changes in the amplitude and shape of the bispectrum hexadecapole, where the linear approximation clearly fails (see Figure 2.4).Consequently, a high degree of agreement between the linear approximation and the exact full model is not universally guaranteed. This investigation suggests that while the linear approximation offers significant improvements in computational speed for bispectrum analysis, it must be applied with caution. To maintain accuracy, fiducial templates used in the modeling should remain relatively close to the actual measurements in terms of α_ϵ values. The required proximity will depend on the strength of the bispectrum monopole signal and is expected to vary between different galaxy samples.These findings are particularly relevant for future large-scale structure surveys aiming to measure the Baryon Acoustic Oscillation (BAO) feature within the galaxy bispectrum. While the computational cost of modeling AP distortions for the monopole can be significantly reduced through this linear model, the bispectrum quadrupole may still require more computationally expensive, direct computations to ensure sufficient accuracy.

In the second part of this thesis, we have performed a comprehensive optimization of the projected correlation function, $w_p(r_p)$, focusing on the selection of the line-of-sight integration limit, $\pi_{\max}$. Using the `AbacusSummit` simulation suite, we evaluated the sensitivity of the clustering signal to HOD and cosmological parameters through the application of the Fisher Information Matrix and a simplified Fisher Information Like Quantity.

Our analysis of the small-box simulations reveals that the optimal $\pi_{\max}$ is not a static value but rather scales approximately linearly with the radial separation, r_p. This trend is most robust for the central galaxy HOD parameters, $M_{\rm cut}$ and σ. While the analysis of satellite parameters (α and κ) remains susceptible to stochastic noise due to their limited impact on the total galaxy population, the overall result suggests that a scale-dependent $\pi_{\max}$ could yield improved constraints compared to the traditional fixed-limit approach.

Furthermore, our investigation into large-box simulations confirmed these findings. While the noise properties of the large-box samples differed—exhibiting smoother derivatives but noisier covariance-derived errors—the underlying linear dependence of optimal $\pi_{\max}$ on the radial bin remained evident. This consistency across different simulation scales underscores the physical relevance of the line-of-sight integration threshold in capturing clustering information while mitigating the damping effects of large-scale averaging.

Finally, we performed a multi-dimensional optimization of HOD parameters across ten distinct cosmologies to identify the configurations that minimize deviance from the base `Planck` (`c000`) cosmology. We found that for cosmological discrimination, higher π_{max} values generally provide better results due to increased averaging, which helps to isolate broader cosmological shifts from localized HOD variations. The optimized parameters detailed in Table 3.1 provide a roadmap for understanding the degeneracies between galaxy bias and cosmological parameters in future surveys.

Collectively, these results suggest that the choice of π_{max} should be carefully tailored to the specific science goals of a survey: lower, scale-dependent values for maximizing HOD information, and higher, fixed values for distinguishing between cosmological models.

Bibliography

[1] Liang Gao et al. The DESI One-Percent Survey: Halo Occupation Distribution of Emission Line Galaxies. *Monthly Notices of the Royal Astronomical Society*, 530(1): 947–965, 2024. doi: 10.1093/mnras/stae1161.

[2] G. Khomeriki and L. Samushia. Mixing of the galaxy bispectrum multipoles under geometric distortions. *Monthly Notices of the Royal Astronomical Society*, 527(3): 5886–5894, 01 2024. doi: 10.1093/mnras/stad3332. URL https://doi.org/10.1093/mnras/stad3332.

[3] C. Alcock and B. Paczynski. An evolution free test for non-zero cosmological constant. , page 358, 1979.

[4] Chris Blake and Karl Glazebrook. Probing Dark Energy Using Baryonic Oscillations in the Galaxy Power Spectrum as a Cosmological Ruler. , 594(2):665–673, September 2003. doi: 10.1086/376983.

[5] Enrique Gaztañaga, Anna Cabré, and Lam Hui. Clustering of luminous red galaxies - IV. Baryon acoustic peak in the line-of-sight direction and a direct measurement of H(z). , 399(3):1663–1680, November 2009. doi: 10.1111/j.1365-2966.2009.15405.x.

[6] Lado Samushia, Will J. Percival, Luigi Guzzo, Yun Wang, Andrea Cimatti, Carlton Baugh, James E. Geach, Cedric Lacey, Elisabetta Majerotto, Pia Mukherjee, and Alvaro Orsi. Effects of cosmological model assumptions on galaxy redshift survey measurements. , 410(3):1993–2002, January 2011. doi: 10.1111/j.1365-2966.2010.17577.x.

[7] E. A. Kazin, A. G. Sánchez, and M. R. Blanton. Improving measurements of H(z) and D_A (z) by analysing clustering anisotropies. , 419:3223–3243, 2012. doi: 10.1111/j.1365-2966.2011.19962.x.

[8] J. Blazek et al. Geometric and dynamic distortions in anisotropic galaxy clustering. , 2014:001, 2014. doi: 10.1088/1475-7516/2014/04/001.

[9] Y.-S. Song, T. Okumura, and A. Taruya. Broadband Alcock-Paczynski test exploiting redshift distortions. , 89:103541, 2014. doi: 10.1103/PhysRevD.89.103541.

[10] A. J. Ross, W. J. Percival, and M. Manera. The information content of anisotropic Baryon Acoustic Oscillation scale measurements. , 451:1331–1340, 2015. doi: 10.1093/mnras/stv966.

[11] C. G. Sabiu and Y.-S. Song. Cosmic distances probed using the BAO ring. *arXiv e-prints*, art. arXiv:1603.02389, 2016. doi: 10.48550/arXiv.1603.02389.

[12] F. Melia and M. López-Corredoira. Alcock-Paczyński test with model-independent BAO data. *International Journal of Modern Physics D*, 26(6):1750055-265, January 2017. doi: 10.1142/S0218271817500559.

[13] Shaun Cole, Will J. Percival, and others.

[14] Daniel J. Eisenstein and others. Detection of the Baryon Acoustic Peak in the Large-Scale Correlation Function of SDSS Luminous Red Galaxies. , 633(2):560–574, November 2005. doi: 10.1086/466512.

[15] S. Alam et al. The clustering of galaxies in the completed SDSS-III Baryon Oscillation Spectroscopic Survey: DR12 sample. , 470:2617–2652, 2017.

[16] Ashley J. Ross, Lado Samushia, Cullan Howlett, Will J. Percival, Angela Burden, and Marc Manera. The clustering of the SDSS DR7 main Galaxy sample - I. A 4 per cent distance measure at z = 0.15. , 449(1):835–847, May 2015. doi: 10.1093/mnras/stv154.

[17] Ashley J. Ross, Florian Beutler, Chia-Hsun Chuang, et al. The clustering of galaxies in the completed SDSS-III Baryon Oscillation Spectroscopic Survey: observational systematics and baryon acoustic oscillations in the correlation function. , 464(1):1168–1191, January 2017. doi: 10.1093/mnras/stw2372.

[18] Julian E. Bautista and journal = keywords = cosmology: dark energy, cosmology: large-scale structure of Universe, cosmology: observations, Astrophysics - Cosmology and Nongalactic Astrophysics year = 2021 month = jan volume = 500 number = 1 pages = 736-762 doi = 10.1093/mnras/staa2800 archivePrefix = arXiv eprint = 2007.08993 primaryClass = astro-ph.CO adsurl = https://ui.adsabs.harvard.edu/abs/2021MNRAS.500..736B adsnote = Provided by the SAO/NASA Astrophysics Data System others, title = "The completed SDSS-IV extended Baryon Oscillation Spectroscopic Survey: measurement of the BAO and growth rate of structure of the luminous red galaxy sample from the anisotropic correlation function between redshifts 0.6 and 1".

[19] Anand Raichoor, Arnaud de Mattia, Ashley J. Ross, et al. The completed SDSS-IV extended Baryon Oscillation Spectroscopic Survey: large-scale structure catalogues and measurement of the isotropic BAO between redshift 0.6 and 1.1 for the Emission Line Galaxy Sample. , 500(3):3254–3274, January 2021. doi: 10.1093/mnras/staa3336.

[20] Jiamin Hou, Ariel G. Sánchez, Ashley J. Ross, et al. The completed SDSS-IV extended Baryon Oscillation Spectroscopic Survey: BAO and RSD measurements from anisotropic clustering analysis of the quasar sample in configuration space between redshift 0.8 and 2.2. , 500(1):1201–1221, January 2021. doi: 10.1093/mnras/staa3234.

[21] Hélion du Mas des Bourboux, James Rich, Andreu Font-Ribera, et al. The Completed SDSS-IV Extended Baryon Oscillation Spectroscopic Survey: Baryon Acoustic Oscillations with Lyα Forests. , 901(2):153, October 2020. doi: 10.3847/1538-4357/abb085.

[22] Q. Mao et al. Cosmic Voids in the SDSS DR12 BOSS Galaxy Sample: The Alcock-Paczynski Test. , 835:160, 2017. doi: 10.3847/1538-4357/835/2/160.

[23] T. Endo, H. Tashiro, and A. J. Nishizawa. The Alcock Paczynski test with voids in 21 cm intensity field. , 499:587–596, 2020. doi: 10.1093/mnras/staa2822.

[24] N. Hamaus et al. Euclid: Forecasts from RSD and the Alcock-Paczynski test with cosmic voids. , 658:A20, 2022. doi: 10.1051/0004-6361/202142073.

[25] D. J. Paz et al. Guess the cheese flavour by the size of its holes: popcorn voids abundance. , 522:2553–2569, 2023. doi: 10.1093/mnras/stad1146.

[26] A. Variu et al. Cosmic void exclusion models and their impact on the distance scale measurements. , 521:4731–4749, 2023. doi: 10.1093/mnras/stad813.

[27] S. Nadathur et al. Beyond BAO: Improving cosmological constraints from BOSS data with void-galaxy cross-correlation. , 100:023504, 2019. doi: 10.1103/PhysRevD.100.023504.

[28] C. M. Correa et al. Non-fiducial cosmological test from geometrical and dynamical distortions around voids. , 485:5761–5772, 2019. doi: 10.1093/mnras/stz821.

[29] S. Nadathur et al. Testing Low-Redshift Cosmic Acceleration with Large-Scale Structure. , 124:221301, 2020. doi: 10.1103/PhysRevLett.124.221301.

[30] C. Zhao et al. Improving BAO measurement with the combination of cosmic voids and galaxies. , 491:4554–4572, 2020. doi: 10.1093/mnras/stz3339.

[31] C. M. Correa et al. Redshift-space effects in voids and their impact on cosmological tests - II. , 509:1871–1884, 2022. doi: 10.1093/mnras/stab3070.

[32] A. Woodfinden et al. Cosmic expansion and growth rate of structure from voids in the SDSS (z = 0.07–1.0). , 516:4307–4323, 2022. doi: 10.1093/mnras/stac2475.

[33] A. Woodfinden et al. Cosmological measurements from void-galaxy and galaxy-galaxy clustering in the SDSS. , 523:6360–6370, 2023. doi: 10.1093/mnras/stad1725.

[34] R. Mauland et al. The void-galaxy cross-correlation function with massive neutrinos and modified gravity. , 674:A185, 2023. doi: 10.1051/0004-6361/202346287.

[35] S. Radinović et al. Euclid: Cosmology forecasts from the void-galaxy cross-correlation function with reconstruction. *arXiv e-prints*, art. arXiv:2302.05302, 2023. doi: 10.48550/arXiv.2302.05302.

[36] G. E. Addison, G. Hinshaw, and M. Halpern. Cosmological constraints from BAO and clustering of large-scale structure. , 436:1674–1683, 2013. doi: 10.1093/mnras/stt1687.

[37] A. Cuceu et al. Cosmology beyond BAO from the 3D distribution of the Lyman-α forest. , 506:5439–5450, 2021. doi: 10.1093/mnras/stab1999.

[38] A. Cuceu et al. The Alcock-Paczyński effect from Lyman-α forest correlations. , 523:3773–3790, 2023.

[39] S. Naoz and R. Barkana. Detecting early galaxies through their 21-cm signature. , 385:L63–L67, 2008. doi: 10.1111/j.1745-3933.2008.00434.x.

[40] J. S. B. Wyithe and A. Loeb. The 21-cm power spectrum after reionization. , 397:1926–1934, 2009. doi: 10.1111/j.1365-2966.2009.15019.x.

[41] L. Wolz et al. Intensity mapping cross-correlations II: HI halo models including shot noise. , 484:1007–1020, 2019. doi: 10.1093/mnras/sty3142.

[42] J. L. Bernal et al. User's guide to extracting cosmological information from line-intensity maps. , 100:123522, 2019. doi: 10.1103/PhysRevD.100.123522.

[43] P. S. Soares et al. Power spectrum multipole expansion for H I intensity mapping experiments. , 502:2549–2564, 2021. doi: 10.1093/mnras/stab027.

[44] Steven Cunnington, Catherine Watkinson, and Alkistis Pourtsidou. The H I intensity mapping bispectrum including observational effects. , 507(2):1623–1639, October 2021. doi: 10.1093/mnras/stab2200.

[45] A. Rubiola, S. Cunnington, and S. Camera. Baryon acoustic oscillations from H I intensity mapping: importance of cross-correlations. , 516:5454–5470, 2022. doi: 10.1093/mnras/stac2484.

[46] G. Valogiannis and C. Dvorkin. Going beyond the galaxy power spectrum: An analysis of BOSS data with wavelet scattering transforms. , 106:103509, 2022. doi: 10.1103/PhysRevD.106.103509.

[47] D. K. Ramanah et al. Cosmological inference from Bayesian forward modelling of deep redshift surveys. , 621:A69, 2019. doi: 10.1051/0004-6361/201834117.

[48] K. Moriwaki, T. Nishimichi, and N. Yoshida. Machine learning for observational cosmology. *Reports on Progress in Physics*, 86:076901, 2023. doi: 10.1088/1361-6633/acd2ea.

[49] R. Scoccimarro. The Bispectrum: From Theory to Observations. , 544:597–615, 2000. doi: 10.1086/317248.

[50] Emiliano Sefusatti, Martín Crocce, Sebastián Pueblas, and Román Scoccimarro. Cosmology and the bispectrum. , 74(2):023522, July 2006. doi: 10.1103/PhysRevD.74.023522.

[51] P. Gagrani and L. Samushia. Information Content of the Angular Multipoles of Redshift-Space Galaxy Bispectrum. , 467:928–935, 2017. doi: 10.1093/mnras/stx135.

[52] Naonori S. Sugiyama, Shun Saito, Florian Beutler, and Hee-Jong Seo. A complete FFT-based decomposition formalism for the redshift-space bispectrum. , 484(1):364–384, March 2019. doi: 10.1093/mnras/sty3249.

[53] Joyce Byun, Andrea Oddo, Cristiano Porciani, and Emiliano Sefusatti. Towards cosmological constraints from the compressed modal bispectrum: a robust comparison of real-space bispectrum estimators. , 2021(3):105, March 2021. doi: 10.1088/1475-7516/2021/03/105.

[54] Mike Shengbo Wang, Florian Beutler, and Naonori S. Sugiyama. Triumvirate: A Python/C++ package for three-point clustering measurements. *arXiv e-prints*, art. arXiv:2304.03643, April 2023. doi: 10.48550/arXiv.2304.03643.

[55] Victoria Yankelevich and Cristiano Porciani. Cosmological information in the redshift-space bispectrum. , 483(2):2078–2099, February 2019. doi: 10.1093/mnras/sty3143.

[56] Naonori S. Sugiyama, Shun Saito, Florian Beutler, and Hee-Jong Seo. Perturbation theory approach to predict the covariance matrices of the galaxy power spectrum and bispectrum in redshift space. , 497(2):1684–1711, September 2020. doi: 10.1093/mnras/staa1940.

[57] Joyce Byun and Elisabeth Krause. Modal compression of the redshift-space galaxy bispectrum. , August in press. doi: 10.1093/mnras/stac2313.

[58] M. Tsedrik et al. Interacting dark energy from the joint analysis of the power spectrum and bispectrum multipoles with the EFTofLSS. , 520:2611–2632, 2023. doi: 10.1093/mnras/stad260.

[59] A. Mazumdar, D. Sarkar, and S. Bharadwaj. Quantifying the RSD of the bispectrum III: detection prospects of multipole moments. , 520:2534–2546, 2023. doi: 10.1093/mnras/stad219.

[60] Z. Slepian et al. Detection of BAO features in the 3PCF of SDSS BOSS DR12 CMASS galaxies. , 469:1738–1751, 2017. doi: 10.1093/mnras/stx488.

[61] Z. Slepian et al. The large-scale three-point correlation function of the SDSS BOSS DR12 CMASS galaxies. , 468:1070–1083, 2017. doi: 10.1093/mnras/stw3234.

[62] D. W. Pearson and L. Samushia. A Detection of the Baryon Acoustic Oscillation features in the SDSS BOSS DR12 Galaxy Bispectrum. , 478:4500–4512, 2018. doi: 10.1093/mnras/sty1266.

[63] Jayashree Behera et al. Modelling the bao feature in bispectrum. *Monthly Notices of the Royal Astronomical Society*, 531:3326–3335, 2024. doi: 10.1093/mnras/stae1161.

[64] R. Scoccimarro. Redshift-space distortions, pairwise velocities, and nonlinearities. , 70:083007, 2004. doi: 10.1103/PhysRevD.70.083007.

[65] H. Gil-Marín et al. RSD measurement from the power spectrum and bispectrum of the DR12 BOSS galaxies. , 465:1757–1788, 2017. doi: 10.1093/mnras/stw2679.

[66] Andrea Oddo, Emiliano Sefusatti, Cristiano Porciani, Pierluigi Monaco, and Ariel G. Sánchez. Toward a robust inference method for the galaxy bispectrum: likelihood function and model selection. , 2020(3):056, March 2020. doi: 10.1088/1475-7516/2020/03/056.

[67] N. S. Sugiyama et al. Towards a self-consistent analysis of the anisotropic galaxy correlation functions. , 501:2862–2896, 2021.

[68] O. H. E. Philcox and M. M. Ivanov. BOSS DR12 full-shape cosmology from power spectrum and bispectrum monopole. , 105:043517, 2022. doi: 10.1103/PhysRevD.105.043517.

[69] Naonori S. Sugiyama, Daisuke Yamauchi, Tsutomu Kobayashi, Tomohiro Fujita, Shun Arai, Shin'ichi Hirano, Shun Saito, Florian Beutler, and Hee-Jong Seo. First test of the consistency relation for the large-scale structure using the anisotropic three-point

correlation function of BOSS DR12 galaxies. , 524(2):1651–1667, September 2023. doi: 10.1093/mnras/stad1935.

[70] Anton Chudaykin, Mikhail M. Ivanov, and Oliver H. E. Philcox. Reanalyzing desi dr1. i. lambda cdm constraints from the power spectrum and bispectrum. *Physical Review D*, 2026.

[71] Anton Chudaykin, Mikhail M. Ivanov, and Oliver H. E. Philcox. Reanalyzing desi dr1. iii. constraints on inflation from galaxy power spectra and bispectra. *Physical Review D*, 2026.

[72] DESI Collaboration. First detection of the bao signal from the desi dr1 sample of luminous red galaxies in the 3-point correlation function. *Preprint*, 2026.

[73] Jennifer E. Pollack, Robert E. Smith, and Cristiano Porciani. Modelling large-scale halo bias using the bispectrum. , 420(4):3469–3489, March 2012. doi: 10.1111/j.1365-2966.2011.20279.x.

[74] Zachary Slepian, Daniel J. Eisenstein, et al.

[75] V. Yankelevich et al. The halo bispectrum as a sensitive probe of massive neutrinos and baryon physics. , 521:1448–1461, 2023. doi: 10.1093/mnras/stad571.

[76] M. Gatti et al. Insensitivity to baryonic effects at minimum smoothing scales using higher-order statistics. *Monthly Notices of the Royal Astronomical Society*, 2024.

[77] E. Sefusatti, M. Crocce, and V. Desjacques. The matter bispectrum in N-body simulations with non-Gaussian initial conditions. , 406(2):1014–1028, August 2010. doi: 10.1111/j.1365-2966.2010.16723.x.

[78] Joyce Byun, Nishant Agarwal, Rachel Bean, and Richard Holman. Looking for non-Gaussianity in all the right places: A new basis for nonseparable bispectra. , 91(12): 123518, June 2015. doi: 10.1103/PhysRevD.91.123518.

[79] A. Moradinezhad Dizgah et al. Primordial non-Gaussianity from biased tracers: power spectrum and bispectrum analysis. , 2021:015, 2021. doi: 10.1088/1475-7516/2021/05/015.

[80] Dionysios Karagiannis, Roy Maartens, José Fonseca, Stefano Camera, and Chris Clarkson. Multi-tracer power spectra and bispectra: Formalism. *arXiv e-prints*, art. arXiv:2305.04028, May 2023. doi: 10.48550/arXiv.2305.04028.

[81] William R. Coulton, Oliver H. E. Philcox, and Francisco Villaescusa-Navarro. The impact of non-gaussian primordial tails on cosmological observables. *Physical Review D*, 2024.

[82] S. J. Rossiter, S. Camera, C. Clarkson, and R. Maartens. Decoupling local primordial non-gaussianity from relativistic effects in the galaxy bispectrum. *Monthly Notices of the Royal Astronomical Society*, 2025.

[83] Sourav Pal et al. Redshift-space galaxy bispectrum in presence of massive neutrinos: a multipole expansion approach for euclid. *Monthly Notices of the Royal Astronomical Society*, 542:223–239, 2025.

[84] J. N. Fry and P. J. E. Peebles. Statistical analysis of catalogs of extragalactic objects. IX. The four-point galaxy correlation function. , 221:19–33, April 1978. doi: 10.1086/156001.

[85] Davide Gualdi, Sergi Novell, Héctor Gil-Marín, and Licia Verde. Matter trispectrum: theoretical modelling and comparison to N-body simulations. , 2021(1):015, January 2021. doi: 10.1088/1475-7516/2021/01/015.

[86] Eve M. Vavagiakis et al. The atacama cosmology telescope: Reionization ksz trispectrum methodology and limits. *Monthly Notices of the Royal Astronomical Society*, 2024.

[87] Oliver H. E. Philcox. Optimal estimation of the binned mask-free trispectrum on the full sky. *Physical Review D*, 2026.

[88] Oliver H. E. Philcox and Julia Ereza. Parity-odd power spectra: Concise statistics for cosmological parity violation. *Monthly Notices of the Royal Astronomical Society*, 533: 2582–2598, 2024.

[89] Oliver H. E. Philcox et al. Parity-violating scalar trispectrum from helical primordial magnetic fields. *ResearchGate*, 2026.

[90] W. J. Handley, M. P. Hobson, and A. N. Lasenby. POLYCHORD: next-generation nested sampling. , 453:4384–4398, 2015. doi: 10.1093/mnras/stv1911.

[91] J. Zuntz, M. Paterno, E. Jennings, D. Rudd, A. Manzotti, S. Dodelson, S. Bridle, S. Sehrish, and J. Kowalkowski. CosmoSIS: Modular cosmological parameter estimation. *Astronomy and Computing*, 12:45–59, September 2015. doi: 10.1016/j.ascom. 2015.05.005.

[92] T. Brinckmann and J. Lesgourgues. MontePython 3: Boosted MCMC sampler and other features. *Physics of the Dark Universe*, 24:100260, 2019. doi: 10.1016/j.dark. 2018.100260.

[93] J. Torrado and A. Lewis. Cobaya: code for Bayesian analysis of hierarchical physical models. , 2021:057, 2021. doi: 10.1088/1475-7516/2021/05/057.

[94] N. Padmanabhan and M. White. Constraining anisotropic baryon oscillations. , 77: 123540, 2008.

[95] Takahiko Matsubara. The correlation function in redshift space: General formula with wide-angle effects and cosmological distortions. *The Astrophysical Journal*, 535(1): 1–23, may 2000. doi: 10.1086/308827. URL https://doi.org/10.1086%2F308827.

[96] Maresuke Shiraishi, Kazuyuki Akitsu, and Teppei Okumura. Alcock-paczynski effects on wide-angle galaxy statistics. *Physical Review D*, 103(12), jun 2021. doi: 10.1103/physrevd.103.123534. URL https://doi.org/10.1103%2Fphysrevd.103.123534.

[97] J. A. Peacock et al. A measurement of the cosmological mass density from clustering in the 2dF Galaxy Redshift Survey. *Nature*, 410:169–173, 2001. doi: 10.1038/35065528.

[98] S. Alam et al. The clustering of galaxies in the completed SDSS-III Baryon Oscillation Spectroscopic Survey: cosmological analysis of the DR12 galaxy sample. *MNRAS*, 470:2617–2652, 2017. doi: 10.1093/mnras/stx721.

[99] M. Davis and P. J. E. Peebles. A survey of galaxy redshifts. V - The two-point position and velocity correlations. *ApJ*, 267:423–441, 1983. doi: 10.1086/160884.

[100] K. B. Fisher et al. The Power Spectrum of the IRAS 1.2 Jy Galaxy Survey. *MNRAS*, 267:1001, 1994. doi: 10.1093/mnras/267.4.1001.

[101] C. Blake and K. Glazebrook. Probing Dark Energy Using Baryonic Oscillations in the Galaxy Power Spectrum as a Cosmological Ruler. *ApJ*, 594:665–673, 2003. doi: 10.1086/376983.

[102] P. Norberg et al. Statistical errors of the two-point galaxy correlation function: what planet are they from? *MNRAS*, 396:19–38, 2009. doi: 10.1111/j.1365-2966.2009.14312.x.

[103] S. Satpathy et al. The clustering of galaxies in the completed SDSS-III Baryon Oscillation Spectroscopic Survey: cosmological implications of the configuration-space clustering of LRG sample. *MNRAS*, 484:1007, 2019. doi: 10.1093/mnras/sty3142.

[104] M. White et al. The Clustering of Galaxies in the SDSS-III Baryon Oscillation Spectroscopic Survey: Luminous Red Galaxies in Data Release 9. *MNRAS*, 446:578–602, 2015. doi: 10.1093/mnras/stu2090.

[105] J. L. Tinker et al. The Redshift-Space Amplitude of Predicted Galaxy Clustering. *ApJ*, 601:1, 2004. doi: 10.1086/380112.

[106] J. L. Bernal et al. User's guide to extracting cosmological information from line-intensity maps. *Phys. Rev. D*, 100:123522, 2019. doi: 10.1103/PhysRevD.100.123522.

[107] T. Brinckmann and J. Lesgourgues. MontePython 3: Boosted MCMC sampler and other features. *Physics of the Dark Universe*, 24:100260, 2019. doi: 10.1016/j.dark.2018.100260.

[108] Sone Yuan et al. The DESI One-Percent Survey: Luminous Red Galaxy Sample Target Selection and HOD Modeling. *The Astrophysical Journal*, 961(1):73, 2024. doi: 10.3847/1538-4357/ad09d6.

[109] Zheng Zheng, Alison L. Coil, and Idit Zehavi. Galaxy Evolution in the Halo Occupation Distribution Framework of Galaxy Clustering. *The Astrophysical Journal*, 667:760–779, 2007. doi: 10.1086/521074.

[110] W. E. Ballinger, J. A. Peacock, and A. F. Heavens. Measuring the cosmological constant with redshift surveys. *Monthly Notices of the Royal Astronomical Society*, 282 (3):877–888, oct 1996. doi: 10.1093/mnras/282.3.877. URL `https://doi.org/10.1093%2Fmnras%2F282.3.877`.

[111] Planck Collaboration, N. Aghanim, and others. Planck 2018 results. VI. Cosmological parameters. , 641:A6, September 2020. doi: 10.1051/0004-6361/201833910.

[112] Antony Lewis and Sarah Bridle. Cosmological parameters from CMB and other data: A Monte Carlo approach. , 66:103511, 2002. doi: 10.1103/PhysRevD.66.103511.

Appendix A

Appendix for Mixing Bispectrum Multipoles

A.1 Wavevector Projections

The primary objective is to derive analytical expressions for the line-of-sight cosines—specifically the angles relative to the z-axis—for the arbitrary triangle configuration depicted in Figure 2.1.We begin by defining a reference triangle within the y-z plane, with the $\mathbf{k}_1$ vector aligned along the positive y-axis. The spatial configuration shown in Figure A.1 is then obtained by applying a sequence of rotations: first, the initial triangle is rotated by an angle ϕ counterclockwise around the y-axis, followed by a second counterclockwise rotation of $/2-\theta_1$ around the x-axis.

Matrices corresponding to these rotations are

$$R_y = \begin{pmatrix} \cos(\phi) & 0 & \sin(\phi) \\ 0 & 1 & 0 \\ -\sin(\phi) & 0 & \cos(\phi) \end{pmatrix}, \tag{A.1}$$

and

$$R_x = \begin{pmatrix} 1 & 0 & 0 \\ 0 & \sin(\theta) & -\cos(\theta) \\ 0 & \cos(\theta) & \sin(\theta) \end{pmatrix}. \tag{A.2}$$

The initial positions of wavevectors are

$$\mathbf{k}_{1,\text{ini}} = (0, k_1, 0)^{\mathrm{T}}, \tag{A.3}$$

$$\mathbf{k}_{2,\text{ini}} = (0, -k_{212}, k_2\nu_{12})^{\mathrm{T}}, \tag{A.4}$$

$$\mathbf{k}_{3,\text{ini}} = (0, -k_{331}, -k_3\nu_{31})^{\mathrm{T}}, \tag{A.5}$$

where θ_{ij} is the angle between vectors k_i and k_j.

After the rotation we get

$$\mathbf{k}_1 = R_x R_y \mathbf{k}_{1,\text{ini}} = (0, k_1\nu_\theta, k_{1\theta})^{\mathrm{T}}, \tag{A.6}$$

$$\mathbf{k}_2 = R_x R_y \mathbf{k}_{2,\text{ini}} = (k_2\nu_{12}\nu_\phi, -k_{2\theta\phi}\nu_{12} - k_{212}\nu_\theta, -k_{212\theta} + k_{2\phi}\nu_{12}\nu_\theta)^{\mathrm{T}},$$

$$\mathbf{k}_3 = R_x R_y \mathbf{k}_{3,\text{ini}} = (-k_3\nu_{31}\nu_\phi, k_{3\theta\phi}\nu_{31} - k_{331}\nu_\theta, -k_{331\theta} - k_{3\phi}\nu_{31}\nu_\theta)^{\mathrm{T}},$$

and the cosine of the angle with respect to the line of sight is

$${}_1 ={}_\theta, \tag{A.7}$$

$${}_2 = -{}_{12\theta} +_\phi \nu_{12}\nu_\theta, \tag{A.8}$$

$${}_3 = -{}_{31\theta} -_\phi \nu_{31}\nu_\theta. \tag{A.9}$$

A.2 Bispectrum projections from Geometry

The wavevector projections established in Appendix A.1 may alternatively be derived through fundamental Euclidean geometry. While the orientation and magnitude of $\mathbf{k}_1$ are trivial by

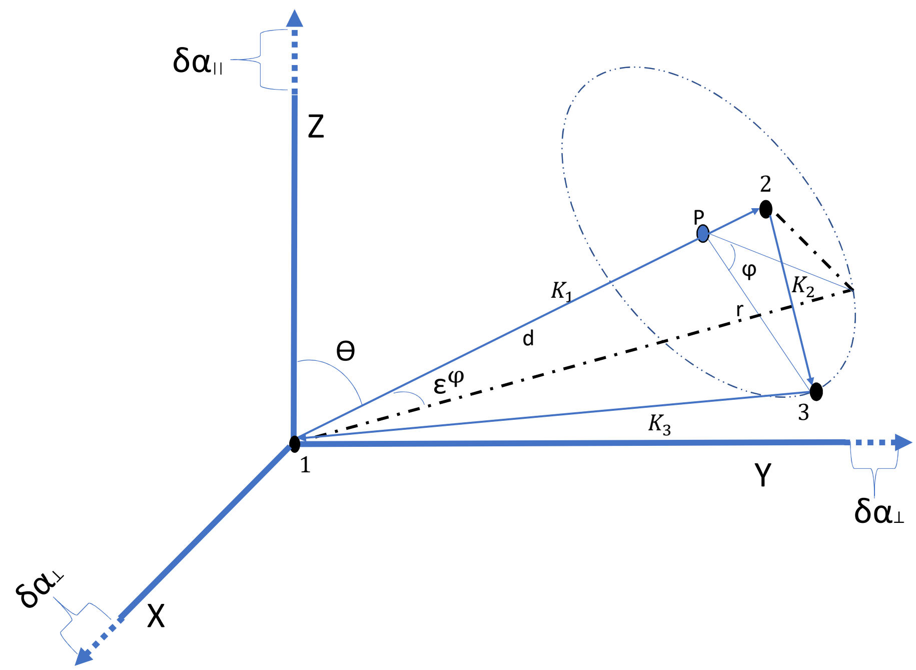

Figure A.1: *The same figure as in Fig.1 for clarity* definition, the distorted wavevectors for the remaining components of the triangle are given by the following expressions:

$$k_2^t = \sqrt{k_2^2 + (\alpha_{||} - 1)^2 k_1} - k_3\sqrt{1 - \frac{r^2\nu_\phi^2}{k_3^2}}\cos(\alpha_\epsilon^\phi + \theta)^2 + (\alpha_\perp - 1)^2 (k_1\nu - k_3\sqrt{1 - \frac{r^2\nu_\phi^2}{k_3^2}}\sin(\alpha_\epsilon^\phi + \theta)^2 + \frac{r^2\nu_\phi^2}{k_3}(\alpha_\perp - 1 \tag{A.10}$$

$$k_3^t = k_3\sqrt{\left(1 - \frac{r^2\sin^2\phi}{k_3^2}\right)\left[\cos^2\left(\alpha_\epsilon^\phi + \theta\right)\alpha_{||}^2 + \sin^2\left(\alpha_\epsilon^\phi + \theta\right)\alpha_\perp^2\right] + \frac{r^2\sin^2\phi}{k_3^2}\alpha_\perp^2}, \tag{A.11}$$

where

$${\alpha_\epsilon}^\phi = \arctan\left(\frac{r\cos\phi}{d}\right) \tag{A.12}$$

and

$$\xi^\phi = \arctan\left(\frac{r\cos\phi}{k_1 - d}\right) \tag{A.13}$$

To linear order in small distortions, these becomes

$$\begin{aligned} k_2^t = k_2 + \delta\alpha_{||}\left[k_1 - k_3\sqrt{1 - \frac{r^2\sin^2\phi}{{k_3}^2}}\cos\left(\alpha_\epsilon^\phi + \theta\right)\right] + \\ + \delta\alpha_\perp\left[k_1\nu - k_3\sqrt{1 - \frac{r^2\sin^2\phi}{{k_3}^2}}\sin\left(\alpha_\epsilon^\phi + \theta\right)\right] + \delta\alpha_\perp\frac{r^2\sin^2\phi}{k_2} \end{aligned} \tag{A.14}$$

$$k_3^t = k_3\left(1 - \frac{r^2\sin^2\phi}{k_3^2}\right)\left[\cos^2\left(\alpha_\epsilon^\phi + \theta\right)\delta\alpha_{||} + \sin^2\left(\alpha_\epsilon^\phi + \theta\right)\delta\alpha_\perp\right] + k_3\frac{r^2\sin^2\phi}{k_3^2}\delta\alpha_\perp + k_3 \tag{A.15}$$

Distortions in ϕ are given by

$$\phi^t = \mathrm{asin}\left(\frac{r}{r^t}\sin\phi\left(1 + \delta\alpha_\perp\right)\right), \tag{A.16}$$

where

$$r = \sqrt{{k_3}^2 - d^2}, \tag{A.17}$$

and

$$d = \frac{{k_1}^2 + {k_3}^2 - {k_2}^2}{2k_1} \tag{A.18}$$

The distortions in r to linear order are

$$\frac{r}{r^t} = 1 + \delta k_1 - \frac{1}{r^2 k_1^2} \left[\sum_{i,j}^{i \neq j} k_i^2 k_j^2 \delta k_j - \sum_{i=1}^{3} k_i^4 \delta k_i \right] \tag{A.19}$$

which results in the following linearized expression for the ϕ -

$$\phi^{\mathrm{t}} = \phi + \tan\phi \left(\delta\alpha_\perp + \delta k_1 - \frac{1}{r^2 k_1^2} \left[\sum_{i,j}^{i \neq j} k_i^2 k_j^2 \delta k_j - \sum_{i=1}^{3} k_i^4 \delta k_i \right] \right). \tag{A.20}$$

For equilateral configurations, with $k_1 = k_2 = k_3 = K$, the equations above simplify further to

$$k_1^{\mathrm{t}} = K(1 +^2 \delta\alpha_{||} + \nu^2 \delta\alpha_\perp) \tag{A.21}$$

$$\begin{aligned} k_2^t = K + \delta\alpha_{||} & \left[K - K\sqrt{1 - \frac{3\sin^2\phi}{4}} \left(\frac{}{\sqrt{1 + 3\cos^2\phi}} - \frac{\nu\sqrt{3}\cos\phi}{\sqrt{1 + 3\cos^2\phi}} \right) \right] \\ + \delta\alpha_\perp & \left[K\nu - K\sqrt{1 - \frac{3\sin^2\phi}{4}} \left(\frac{\sqrt{3}\cos\phi}{\sqrt{1 + 3\cos^2\phi}} + \frac{\nu}{\sqrt{1 + 3\cos^2\phi}} \right) \right] + \delta\alpha_\perp K \frac{\sin^2\phi}{4} \end{aligned} \tag{A.22}$$

$$k_3^{\mathrm{t}} = K\left(1 - \frac{3\sin^2\phi}{4}\right) \left[\left(\frac{}{\sqrt{1 + 3\cos^2\phi}} - \frac{\nu\sqrt{3}\cos\phi}{\sqrt{1 + 3\cos^2\phi}} \right)^2 \delta\alpha_{||} + \left(\frac{\sqrt{3}\cos\phi}{\sqrt{1 + 3\cos^2\phi}} + \frac{\nu}{\sqrt{1 + 3\cos^2\phi}} \right)^2 \delta\alpha \right. \tag{A.23}$$

$$+ K\frac{\sin^2\phi}{4}\delta\alpha_\perp + K$$

$$\phi^t = \arctan\left(\sin\phi\left(1+\delta\alpha_\perp+\delta k_1-\frac{2}{3}(\delta k_1+\delta k_2+\delta k_3)\right)\right) \tag{A.24}$$

We verified that when the results derived in Appendix A.1 are combined with Eqs. 2.15–2.17 the numerical results are identical to the outcome of the formulas derived in this section.

A.3 Computing Model Power Spectrum And Bispectrum

To perform the validation tests illustrated in Figures 2.2 and 2.3, we employ linear perturbation theory to model the power spectrum and bispectrum[49;51].The process begins with the computation of the linear matter power spectrum, $P_{\text{lin}}(k)$, utilizing the `CAMB` software suite[112]. The corresponding galaxy power spectrum is subsequently modeled as follows:

$$P(k) = \left(b_1 + f^2\right) P_{\text{lin}}(k), \tag{A.25}$$

where b_1 and f are free parameters. We compute the bispectrum using

$$B\left(k_1, k_2, k_3\right) = 2Z_1(_1)Z_1(_2)Z_2(\mathbf{k}_1, \mathbf{k}_2)P_{\text{lin}}(k_1)P_{\text{lin}}(k_2) + \text{cyclic terms} \tag{A.26}$$

where

$$Z_1() = \left(b_1 + f^2\right) \tag{A.27}$$

$$Z_2(\mathbf{k}_1, \mathbf{k}_2) = \left\{\frac{b_2}{2} + b_1 F_2(\mathbf{k}_1, \mathbf{k}_2) + f_3^2 G_2(\mathbf{k}_1, \mathbf{k}_2) - \frac{f_3 k_3}{2}\left[\frac{1}{k_1}(b_1 + f_2^2) + \frac{2}{k_2}(b_1 + f_1^2)\right]\right\} \tag{A.28}$$

$$F_2(k_1, k_2) = \frac{5}{7} + \frac{\mathbf{k}_1 \cdot \mathbf{k}_2}{2k_1 k_2}\left(\frac{k_1}{k_2} + \frac{k_2}{k_1}\right) + \frac{2}{7}\left(\frac{\mathbf{k}_1 \cdot \mathbf{k}_2}{2k_1 k_2}\right)^2 \tag{A.29}$$

$$G_2(k_1, k_2) = \frac{3}{7} + \frac{\mathbf{k}_1 \cdot \mathbf{k}_2}{2k_1 k_2}\left(\frac{k_1}{k_2} + \frac{k_2}{k_1}\right) + \frac{4}{7}\left(\frac{\mathbf{k}_1 \cdot \mathbf{k}_2}{2k_1 k_2}\right)^2. \tag{A.30}$$

Cyclic terms are computed by permuting the indices (replacing 1 and 2 by 2 and 3, and then by 3 and 1 in the above equations).

Appendix B

Projected Correlation Function Optimization For QSO at redshift $z = 1.4$

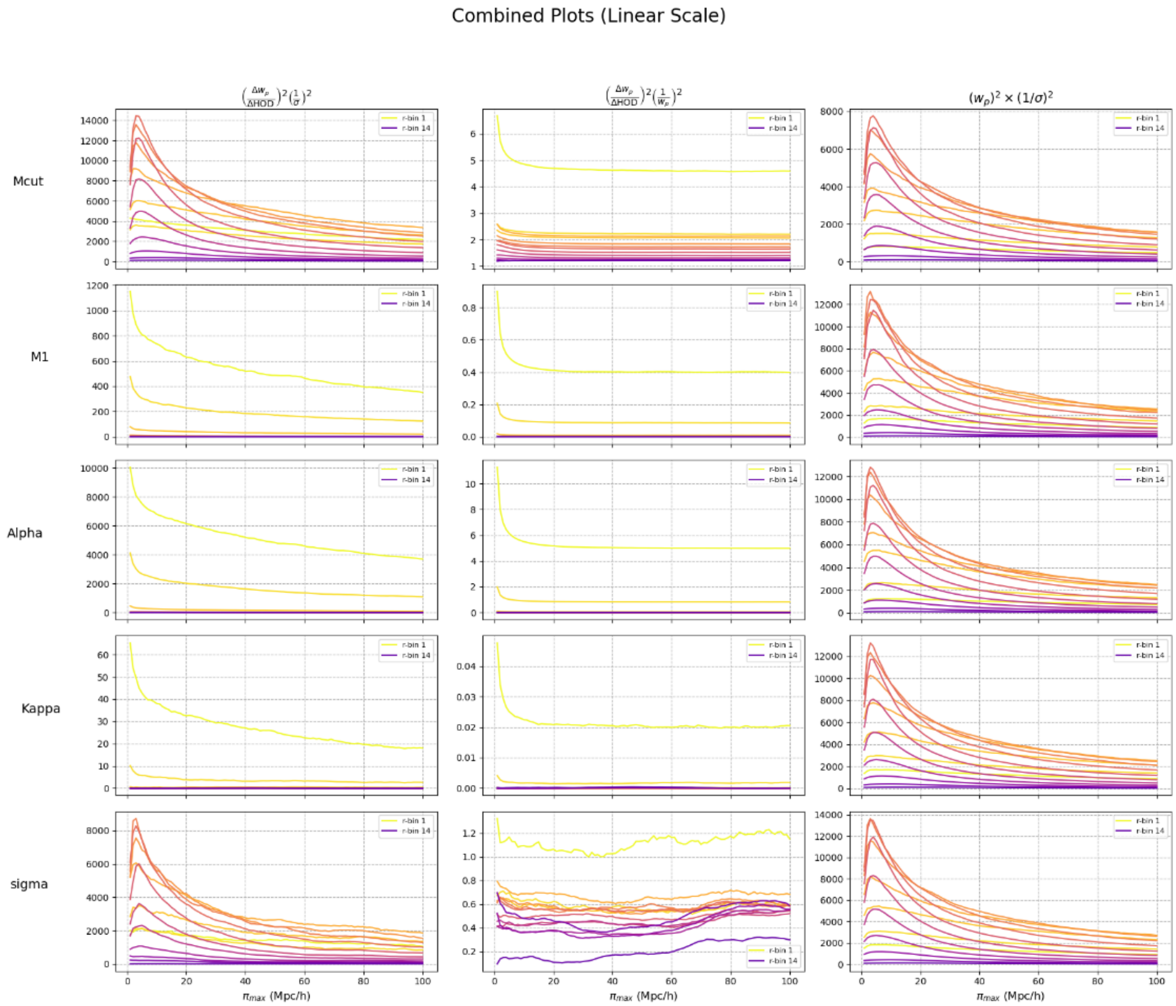

Figure B.1: *For QSO, at redshift $z = 1.4$. The results are similar, however here the difference between optimal π_{max} for different bins is much harder to distinguish, however still present.*